# Particle Physics at CERN

*Annual Report 2010*

(SNF grants 200020-124377 and 206620-134620)

E. Aguiló, Y. Allkofer, C. Amsler, A. Benelli, V. Boccone, W. Creus, S. de Visscher, A. Ferella, M. Ivova Rikova, B. Millán Mejías, P. Otyugova, C. Regenfus, P. Robmann, J. Rochet, T. Rommerskirchen, A. Schmidt, L. Scotto Lavina, J. Storey and M. Walter

V. Chiochia, C. Favaro, A. Jaeger, H. Snoek and M. Verzetti

April 20, 2011

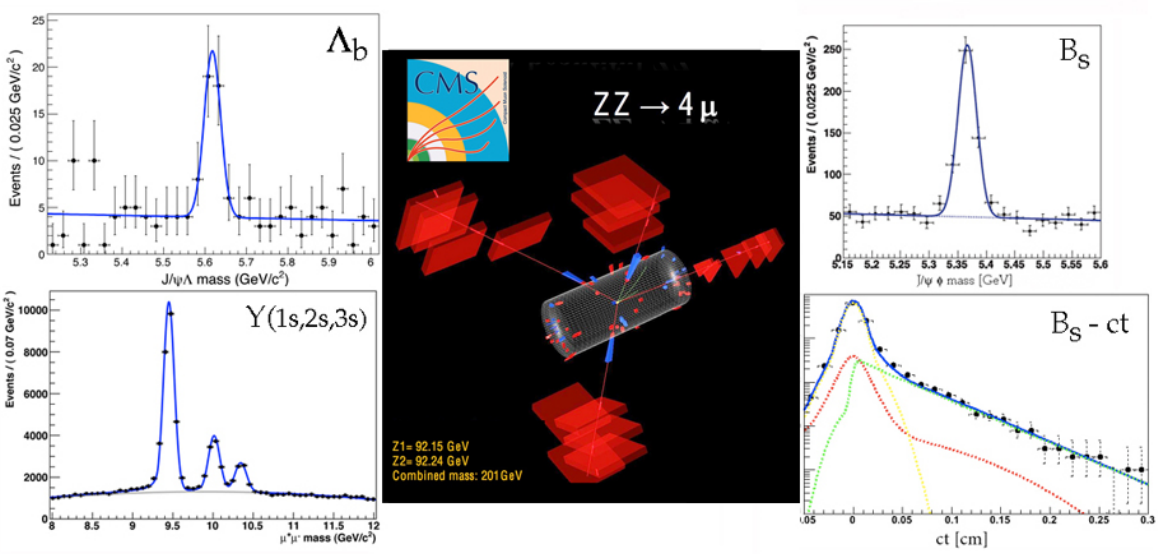


**Physik-Institut der Universität Zürich**
Winterthurerstrasse 190, CH-8057 Zürich, Switzerland

# Contents



This report covers the activities of the Zurich group at CERN on CMS, the DIRAC and the ArDM experiments between 1 April 2010 and 31 March 2011. It does not include the activity of one of us (C. A.) contributing to the "Review of Particle Physics" (Particle Data Group). Further details on the group activities and publication reprints can be obtained from our home page, see http://cern.ch/unizh/.

Cover picture: Center: $Z^0Z^0 \to 4\mu$-event with CMS at 7 TeV. Left: The $\Lambda_b$ observed in the $J/\psi\Lambda$-invariant mass distribution (top) and the $\Upsilon$-sequence reconstructed in the two-muon decay channel (bottom); Right: The $B_s$ observed in the $J/\psi\ \phi$-invariant mass plot (top) with its decay length distribution (bottom).

# 1 Particle physics with CMS

E. Aguiló, C. Amsler, S. de Visscher, M. Ivova, B. Millán Mejías, P. Otyugova, C. Regenfus, P. Robmann, J. Rochet, T. Rommerskirchen, A. Schmidt, and J. Storey

V. Chiochia, C. Favaro, A. Jaeger, H. Snoek, and M. Verzetti

*In collaboration with:*
Paul Scherrer Institut (PSI) and the CMS Collaboration

## 1.1 Introduction

After commissioning with cosmic rays the CMS experiment [1] at the LHC recorded proton collisions in December 2009 at the center of mass energy of 900 GeV. The detector performances had to be verified first by comparing with our current knowledge of the standard model. The mass distributions in fig. 1.1, obtained after various selection cuts, illustrate some of the known particles "rediscovered" by CMS. A run at the unprecedented energy of 7 TeV took place in March – December 2010, collecting about 40 pb$^{-1}$ (see fig. 1.2, left). The data analysis of the 2010 dataset is now well advanced. When writing this report, 41 journal articles by the CMS collaboration had been published or were in print. One of us (V.C.) was Deputy Project Manager of the silicon tracker in 2010 and now chairs the $B$-physics analysis group, that has so far released six journal articles on quarkonium, $B$ mesons and inclusive $b$-quark production measurements. One of us (H.S.) convenes the pixel calibration and reconstruction group.

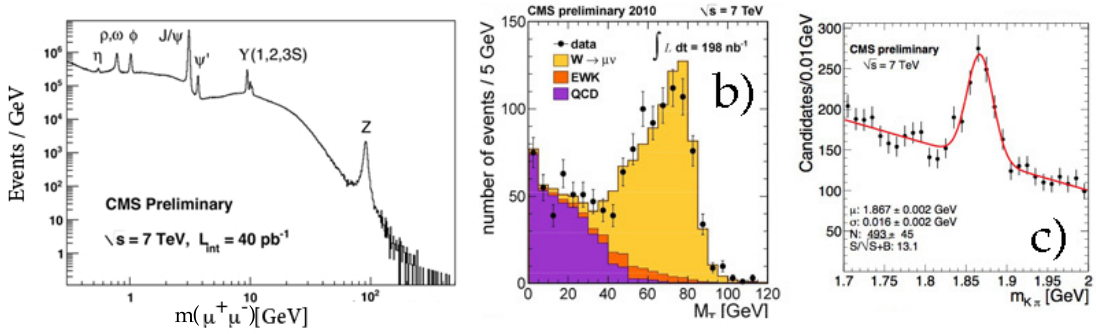


Figure 1.1: *Some of the preliminary results obtained during summer 2010: a) $\mu^+\mu^-$ mass distribution showing the vector mesons and the $Z^0$ peak; b) transverse mass distribution of muons showing the (Jacobian) peak from $W \to \mu\nu$ decay; c) $K^-\pi^+$ mass distribution showing the $D^0$.*

The silicon pixel detector is the innermost component of the CMS experiment. It allows a precise reconstruction of charged particles and the identification of secondary vertices from long-lived particles. The 53 cm long barrel pixel section, with about 48 million channels, consists of three cylindrical layers at radii between 4.4 cm and 10.2 cm. Two endcap disks at each side of the barrel section provide coverage up to large rapidities. Details can be found in various publications such as [2, 3, 4]. Figure 1.2 (right) shows an event with two displaced vertices from $b$ hadron decays.

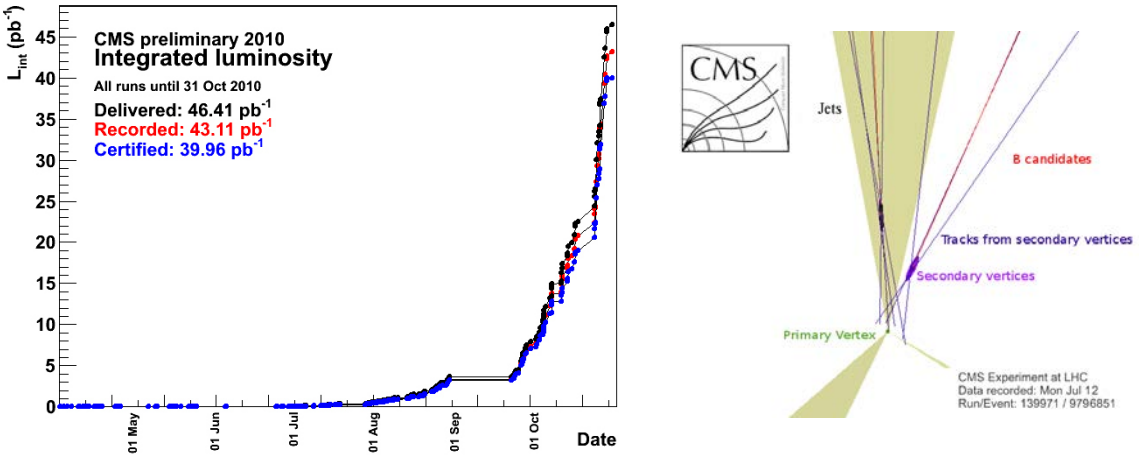


Figure 1.2: *Left: Integrated luminosity in the 2010 run at $\sqrt{s}$ = 7 TeV. Right: CMS event showing two displaced vertices from $B$ hadron decays [5].*

## 1.2 Commissioning of the silicon pixel detector

Our first priority was to measure the pixel detector performance with LHC collisions and to compare with expectations. We performed several important measurements and calibrations, ranging from the detector occupancy to position resolution [6]. The position resolution was improved with the larger data samples collected at $\sqrt{s}$ =7 TeV. The technique was based on pairs of consecutive hits along a trajectory in the overlap region between two adjacent modules within a layer (see last year's annual report). The data were compared to predictions from the detailed PIXELAV simulation [7]. The transverse and longitudinal resolutions are shown in fig.1.3 as a function of cluster length. The agreement between data and prediction is remarkable, demonstrating the excellent understanding of the detector response already in the early phase of its operation.

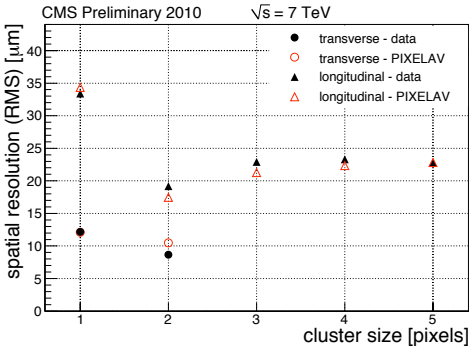


Figure 1.3: *Transverse and longitudinal hit position resolution of the pixel barrel detector. The data (in black) are compared to the prediction from the PIXELAV simulation.*

## 1.3 Improvements to hit and track reconstruction

Searches for the Higgs boson and Supersymmetry depend heavily on the identification of $\tau$ leptons and $b$-quarks. Since the transverse momentum of the $\tau$ jet is large compared to the $\tau$ mass, the decay pions emerge as collimated jets in which individual tracks become inseparable with increasing momentum. Hits in the pixel sensors merge forming broad clusters (in the inner-most pixel layer when the opening angle between two trajectories is below 5 mrad). For a typical 3-prong $\tau$ decay this angle

corresponds to a transverse momentum of 150 GeV/c. Hit merging deteriorates the reconstruction of the $\tau$ mass, thus excellent spatial resolution is needed for $\tau$ reconstruction.

Merged clusters generate peaks in the cluster charge distribution at integer multiples of the minimium ionizing energy deposit. We have therefore developed an algorithm to split the merged cluster. The track impact angle on the sensor is used to compare the observed cluster shapes from the expected ones which were simulated with very high-$p_t$ jets. Figure 1.4 shows the track reconstruction efficiency as a function of transverse momentum and opening angle with the closest neighboring track. The cluster splitting technique (red triangles) recovers 20% of the tracking efficiency at large transverse momenta for which the tracks have close neighbors with opening angles below 5 mrad.

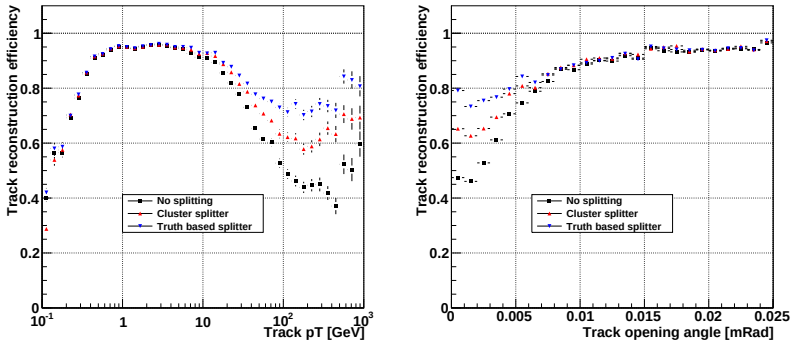


Figure 1.4: *Left: Track reconstruction efficiency as function of transverse momentum for high-$p_t$ jets. The current reconstruction is represented by the black squares. Ideal cluster splitting is given by blue triangles while the performance of our splitting algorithm is represented by red triangles. Right: Track reconstruction efficiency as a function of opening angle with the closest neighboring track.*

We also performed a study to determine the effects that possible misalignments of the tracker detectors would have on the $J/\psi$ lifetime fits (which determine the fraction of $J/\psi$ mesons coming from $B$ decays). The effect of the various misalignments led to a relative error in the $B$-fraction ranging from 0.5 to 9% [8].

## 1.4 Searches for the Higgs boson decaying into $\tau^+\tau^-$

CMS has searched for the neutral Higgs boson[1] decaying into $\tau^+\tau^-$ at $\sqrt{s} = 7$ TeV using 36 pb$^{-1}$ [9]. The reconstructed $\tau^+\tau^-$ mass distribution for leptonic $\tau$ decays is shown in fig. 1.5 (left). There is no evidence for a Higgs boson signal and we set 95% CL upper bounds on the Higgs boson cross section times the $\tau$ pair branching fraction. Furthermore, we can interpret the upper limit in the MSSM parameter space given by the mass of the pseudoscalar state, $m_A$ and the ratio of the vacuum expectation values of the two Higgs doublets, $\tan\beta$, for the benchmark scenario $m_h^{max}$ (fig. 1.5, right). The present results exclude a region in $\tan\beta$ down to values smaller than those excluded by the Tevatron for $m_A < 140$ GeV/c$^2$, and significantly extend the excluded region of MSSM parameter space at larger values of $m_A$.

We are preparing data driven measurements of the $\tau$ identification efficiency and studying $\tau$ tagging performance using different collision pile-up scenarios. Hadronic $\tau$ decays lead mainly to one or

[1] Minimum Supersymmetric Standard Model (MSSM) Higgs.

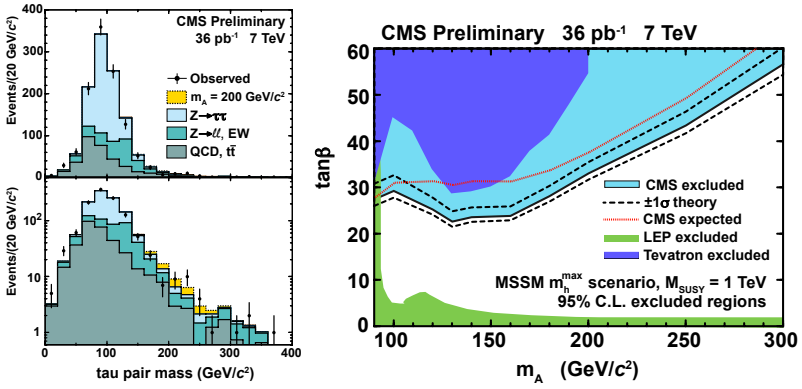


Figure 1.5: *Left: Reconstructed $\tau$ pair invariant mass distribution (linear and logarithmic scales) with the expected backgrounds. The possible contribution from a Higgs boson ($m_A = 200$ GeV/$c^2$) is also shown in yellow. Right: Region in parameter space of* $\tan\beta$ *vs.* $m_A$ *excluded by CMS, the Tevatron and LEP experiments at 95% CL.*

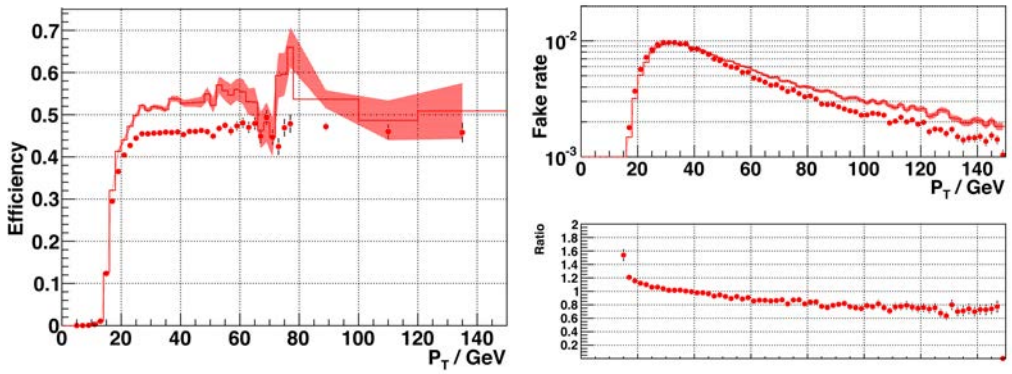


Figure 1.6: *Left: $\tau$ reconstruction efficiency as a function of transverse momentum for two scenarios, corresponding to the 2010 (histogram) and 2011 running conditions (red circles). Right: Fake rate as a function of the $\tau$ transverse momentum.*

three charged pions, with or without neutral pions. The identification algorithm starts with a charged hadron at high transverse momentum, combining with other nearby reconstructed charged hadrons and neutral pions, retaining the combinations consistent with $\tau$ decay kinematics. The most isolated one is then selected. Figure 1.6 shows the identification efficiency and background contamination from Monte Carlo simulation in two luminosity scenarios for the 2010 and 2011 data taking. A loss of efficiency is observed in 2011 due to the increase in pile-up events. We are optimizing the algorithm to cope with the new running conditions and will soon release an updated Higgs exclusion limit for this channel.

## 1.5 $B_s \to J/\psi\,\phi$

The decay $B_s \to J/\psi(\to \mu^+\mu^-)\phi(\to K^+K^-)$ is a benchmark channel for CMS for which we have prepared the corresponding software. We are studying this channel to determine the $B_s$ mass

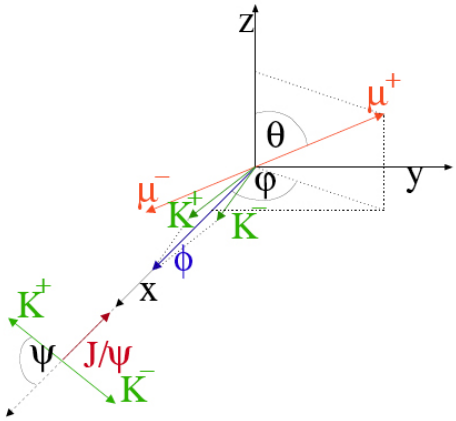


Figure 1.7: *Definition of the angles $\theta, \phi$ and $\psi$ that describe $B_s \to J/\psi\,\phi$ decay.*

and average lifetime of the $B_s^H$ and $B_s^L$ eigenstates. An analysis of the angular correlations can be performed to extract $\Delta\Gamma_s$. Since the expected value for $\Delta\Gamma_s/\Gamma_s$ is small (around 0.2) the mean lives of the two eigenstates are difficult to measure directly from the decay length distribution. However, the two states contribute differently to the angular correlations (fig. 1.7) between the decay particles. We expect to achieve an r.m.s uncertainty of 0.04 on $\Delta\Gamma_s/\Gamma_s$ for an integrated luminosity of about 1 fb$^{-1}$ [10] which should easily be reachable in 2011.

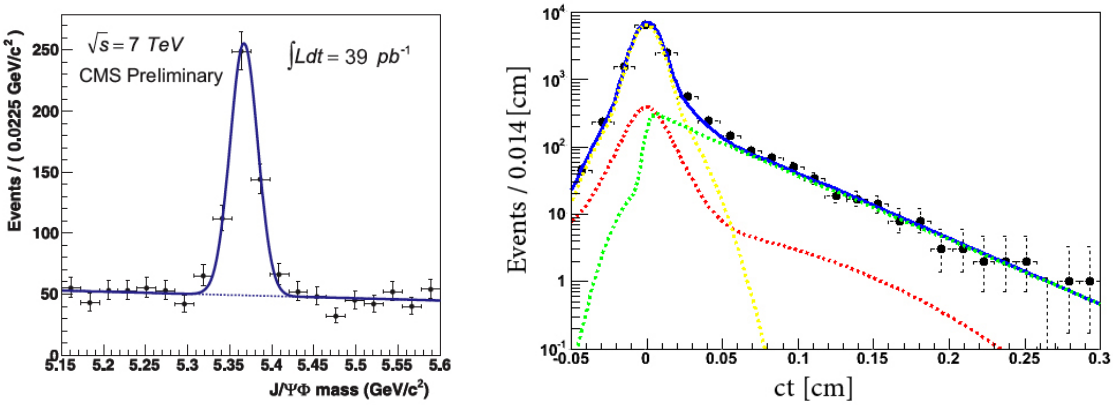


Figure 1.8: *Left: $(\mu^+\mu^-)K^+K^-$ invariant mass for $\sqrt{s} = 7$ TeV and $\mathcal{L} = 39$ pb$^{-1}$ showing the $B_s$ (377 $\pm$ 26 events). Right: Decay length distribution with likelihood fit. The curves in the plot show all contributions (solid blue line), background (red), prompt background (yellow) and signal (green).*

The $B_s$ candidates are selected first with the two-muon trigger, requiring opposite sign muons and reconstructing the $J/\psi$ with a transverse momentum larger than 0.5 GeV/c. The two hadrons (transverse momentum above 0.7 GeV/c) are assumed to be kaons. Their invariant mass is required to be within 10 MeV/c$^2$ of the known $\phi$ mass. A kinematic fit constraining the $J/\psi$ mass and a cut on the $B_s$ decay length ($c\tau/\sigma > 3$) are then applied. Figure 1.8 shows the $B_s$ with an integrated luminosity of 39 pb$^{-1}$, obtained by CMS at 7 TeV. The fitted mass is 5367.0 $\pm$ 1.2 MeV (compared to the PDG value of 5366.3 $\pm$ 0.6 MeV [11]). Figure 1.8 (left) shows the decay length distribution for the $B_s$. A two-dimensional likelihood fit was applied. The result from the fit is $c\tau$ = 454.6 $\pm$ 15.8

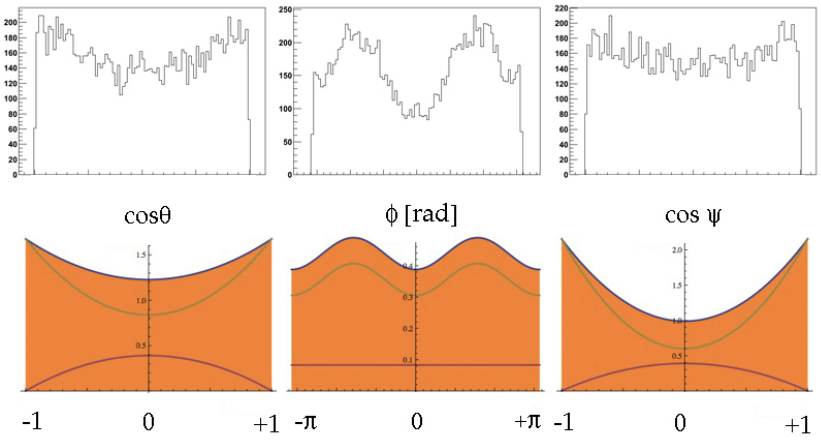


Figure 1.9: *Top: Measured distributions of* $\cos\theta$*,* $\phi$ *and* $\cos\psi$ *obtained with 46 pb*$^{-1}$ *at 7 TeV. Bottom: Predictions for* $CP$*-odd (pink) and* $CP$*-even (green)* $B_s$*-states [10].*

$\mu$m (compared to the PDG value of 425.0 $\pm$ 12.6 $\mu$m).

Figure 1.9 shows our preliminary distributions for the angles $\theta$, $\phi$ and $\psi$ (defined in fig. 1.7) for the data collected so far in 2010 and 2011. The similarities with Monte Carlo simulation using the decay parameters from ref. [10] are quite encouraging.

## 1.6 Study of $b$–baryons

The spectroscopy of heavy baryons is of interest to QCD and to models of the strong interaction [12]. The quark model predicts 56 heavy ground state baryons (with at least one $c$ or $b$-quark). So far only 8 $b$-baryons have been observed, but the evidence often rests on a handful to a few dozen events.

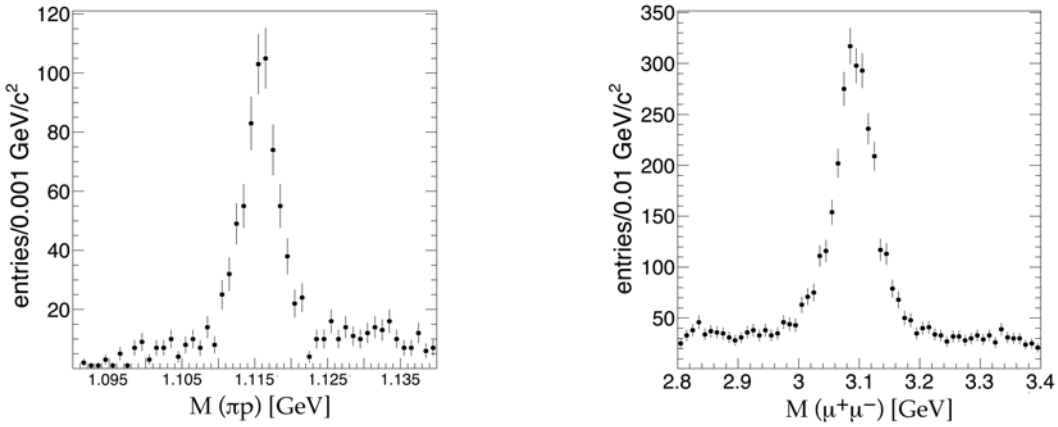


Figure 1.10: *Left:* $\pi p$ *invariant mass distribution showing the* $\Lambda$ *(*$\bar{\Lambda}$*). Right:* $\mu^+\mu^-$ *invariant mass showing the* $J/\psi$*.*

The study of heavy baryons by our group was launched with a study of the neutral $\Lambda_b$ ($udb$). The decay channel $\Lambda_b \to J/\psi\ \Lambda$ with $J/\psi \to \mu^+\mu^-$ and $\Lambda \to \pi^- p$ can be studied at CMS. Both $\Lambda_b$ and $\Lambda$ are long-lived particles, travelling up to several centimeters before decaying (leading to displaced vertices), and muons in the final state which can be triggered on. The $\Lambda$ (fig. 1.10, left) is

combined with the $J/\psi \to \mu^+\mu^-$ (fig. 1.10, right) to form $\Lambda_b$ candidates. Figure 1.11 (left) shows the reconstructed $J/\psi\ \Lambda$ invariant mass after applying a series of cuts (e.g. reasonably large transverse momenta and proper decay length $c\tau(\Lambda) > 1$ cm, $c\tau(\Lambda_b) > 50$ $\mu$m). A clear $\Lambda_b$ peak is observed. These data were collected in 2010 with an integrated luminosity of 40 pb$^{-1}$.

Measurements of the mass and proper decay length of the $\Lambda_b$ are shown fig. 1.11. A maximum likelihood fit was applied with a single Gaussian plus a linear background for the mass distribution, and a Gaussian plus exponential function for the proper decay length. We obtain $M(\Lambda_b) = 5618 \pm 5$ MeV and $c\tau(\Lambda_b) = 379 \pm 33$ $\mu$m (statistical errors only). These results are in agreement with the known values ($5620.2 \pm 1.6$ MeV, resp. $417 \pm 11$ $\mu$m [11]).

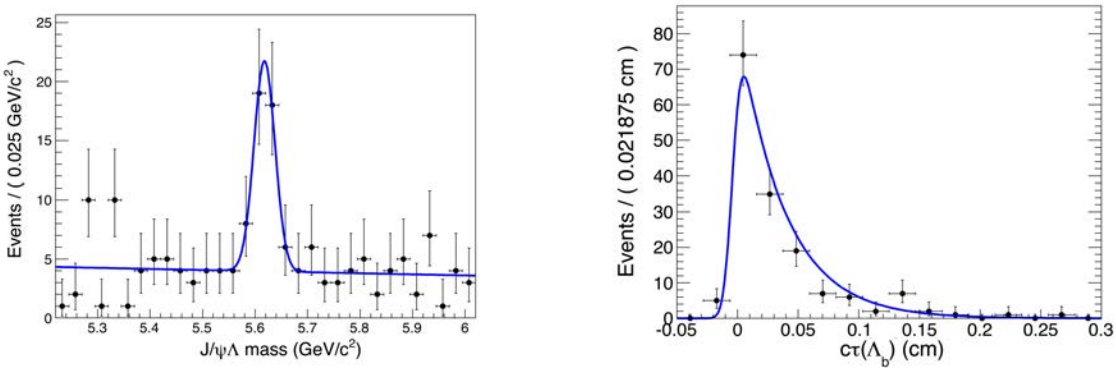


Figure 1.11: *Left: $J/\psi\Lambda$ invariant mass distribution with 40 pb$^{-1}$ of data ($36 \pm 9$ events) with $\Lambda_b$ fit (blue line). Right: Proper decay length distribution of the $\Lambda_b$.*

The reconstructed $\Lambda_b$ candidates are a starting point to search for further heavy baryons, the $\Sigma_b^{(*)+}$ ($uub$) and $\Sigma_b^{(*)-}$ ($ddb$). The dominant decay mode is $\Sigma_b \to \Lambda_b\pi$, a strong decay that takes place at the primary vertex. The selection of the soft pion coming from $\Sigma_b$ is not easy in the dense environment around the primary vertex. Applying loose cuts in view of the still limited statistics, and combining each $\Lambda_b$ candidate with an extra track, leads to four potential peaks from $\Sigma_b$ states. Figure 1.12 shows the reconstructed $Q$-value distribution of the decay $\Sigma_b \to \Lambda_b\pi$ where $Q = M(\Lambda_b\pi) - M(\Lambda_b) - M(\pi)$. The theoretically predicted $Q$-values lie in the range 0.03 – 0.1 GeV [13]. A simultaneous maximum likelihood fit was applied with a smooth function to parametrize the background and a Breit-Wigner distribution convoluted with a Gaussian for each mass peak. Equidistance between the peak mean values were required. Our preliminary measurements are in agreement with theoretical expectations and the measurements by CDF [14]. These early indications of signals from the very first and limited LHC data make the study of $b$-baryons very promising.

Triggers specific to particular processes will be needed as the luminosity increases. CMS reconstructs $b$-hadrons through their decay into a $J/\psi \to \mu^+\mu^-$. Triggering on $J/\psi$ is achieved with the high level trigger on $\mu^+\mu^-$ and the additional requirement that the $J/\psi$ should be emitted from a secondary vertex. However, many channels such as $\Lambda_b \to J/\psi(\to \mu^+\mu-)\Lambda(\to p^+\pi^-)$, $\Xi_b^- \to J/\psi(\to \mu^+\mu-)\Xi^-(\to \Lambda\pi^-)$, $\Omega_b^- \to J/\psi(\to \mu^+\mu-)\Omega^-(\to \Lambda K^-)$ have long-lived particles leading to tertiary vertices far away from the $J/\psi$ vertex, often beyond the pixel detector. The straightforward approach is to select high transverse momentum tracks (proton from $\Lambda$ decay) with large impact parameter with respect to the secondary and primary vertices. A second lower transverse momentum track (e.g. pion from $\Lambda$ decay) is then required. This work is in progress.

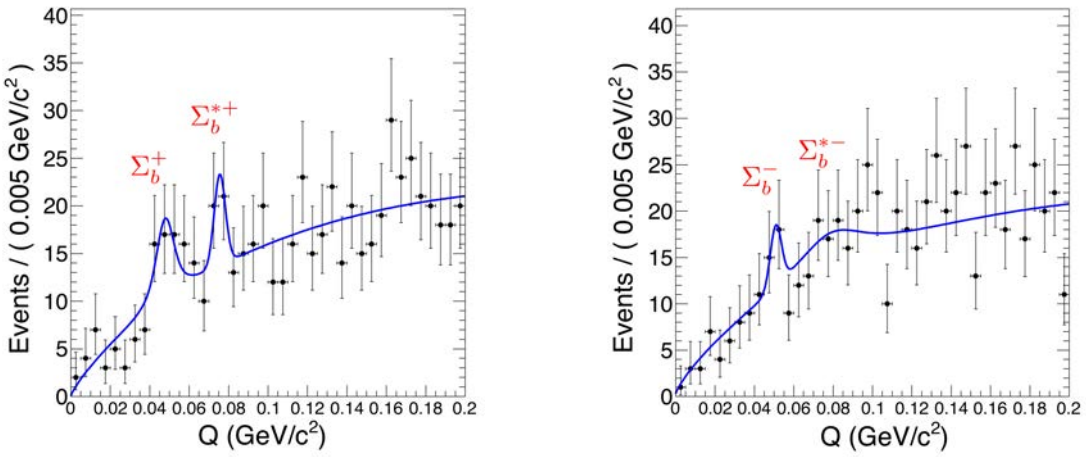


Figure 1.12: *Q-value distribution for $\Sigma_b \to \Lambda_b\pi$ for positive (left) and negative (right) charges from the first 40 pb$^{-1}$ of data. The blue line shows a simultaneous maximum likelihood fit.*

## 1.7 $b$-jet tagging

Identifying jets containing $b$-decays ("b-tagging") is an essential tool for a wide range of topics in and beyond the Standard Model [15]. In CMS $b$-tagging tools have been applied in e.g. measurements of the inclusive $b$- and $t$-quark production cross-sections.

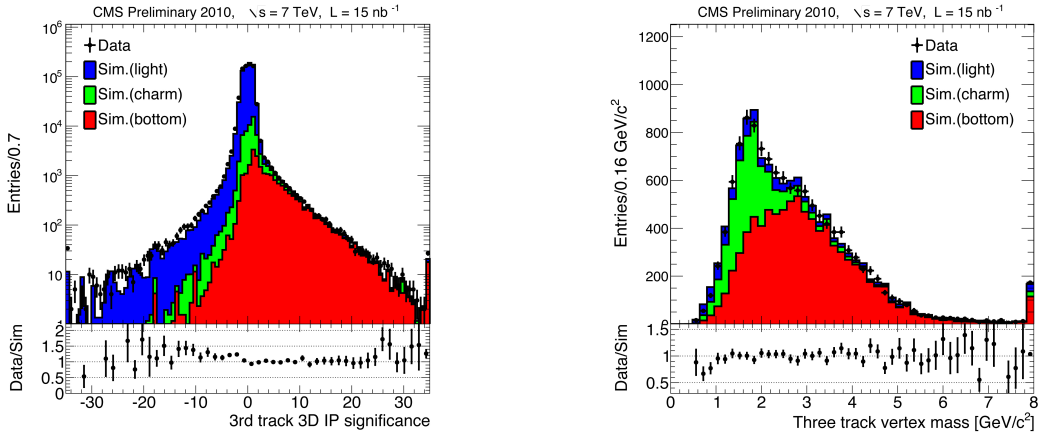


Figure 1.13: *Left: Impact parameter (IP) significance of the third track in a jet (ordered by IP significance). Right: invariant mass of secondary vertices with at least three tracks. The Monte Carlo simulation of light, charm and jets is shown in blue, green and red, while the data are represented as black markers.*

We have been involved in $b$-tagging since many years with one of us (A.S.) coordinating the commissioning of $b$-jet identification with 7 TeV collision data [16]. The crucial device for good $b$-tagging performance is the pixel detector which reconstructs charged tracks close to the proton-proton interaction point. One of the most important quantities is the impact parameter (IP), the distance between the primary proton-proton interaction vertex and the track at their point of closest approach. The IP significance of the third track in a jet is shown in fig. 1.13 (left). The tail in this distribution is quite sensitive to $b$-quarks, and is therefore used as discriminator in a high purity $b$-tagging algorithm.

The secondary vertex from $B$ decays can be reconstructed using the so-called adaptive vertex fitting technique [17]. A secondary vertex with three or more tracks has a high probability of being a $B$ decay vertex. The flight distance which is defined as the separation between the primary and secondary vertices is used in the $b$-tagging algorithm.

Another important quantity is the invariant mass of the secondary vertex, assuming pions. This quantity is shown in Figure 1.13 (right) for vertices with three or more tracks. With the vertex mass one can distinguish between light flavours, charm and beauty. This was used in the measurement of the inclusive $b$ production cross-section [18], the first precision measurement using $b$-tagging in CMS. First results on performance in $b$-tagging have been published [16] but systematic errors are still large. Our group continues to play a leading role in the $b$-tagging group in 2011.

In parallel with CMS studies of the inclusive cross-section for $pp \rightarrow b + X$ we contributed to the study of the angular correlation between pairs of $B$ mesons. We have enhanced the performance of the $b$-tagging algorithm to reconstruct two $b$-jets with close spacial separation. We select events with one secondary vertex each which have similar spatial coordinates (distance smaller than typically $20\mu$m), mix them pairwise and reconstruct them. Events for which both initial secondary vertices are reconstructed in the mixed events are then counted. The efficiency of the vertex finder is calculated as the fraction of the number of secondary vertices in the mixed sample to the corresponding number in both event samples before mixing. The efficiency was studied as a function of vertex separation $\Delta R$, defined as $\sqrt{\Delta\eta^2 + \Delta\phi^2}$, where $\eta$ is the pseudorapidity and $\phi$ the azimuthal angle.

On the other hand, we have predicted the fraction of $b$-quarks produced collinearly or not, that is via gluon-splitting or through flavor creation/excitation, respectively. This study, made with `Pythia` and `Madgraph`, led to a first estimate of the relative importance of the "gluon splitting" peak compared to the back-to-back region mainly due to flavor creation or excitation. This was calculated for different $p_T$ ranges of the leading jet (fig. 1.14, left).

The $\Delta R$ dependence of the double vertex reconstruction efficiency (fig. 1.14, right) shows very good agreement for the shape between data and simulation, with discrepancies below 2% [19]. Efficiencies of typically 90% for the double vertex reconstruction can be reached.

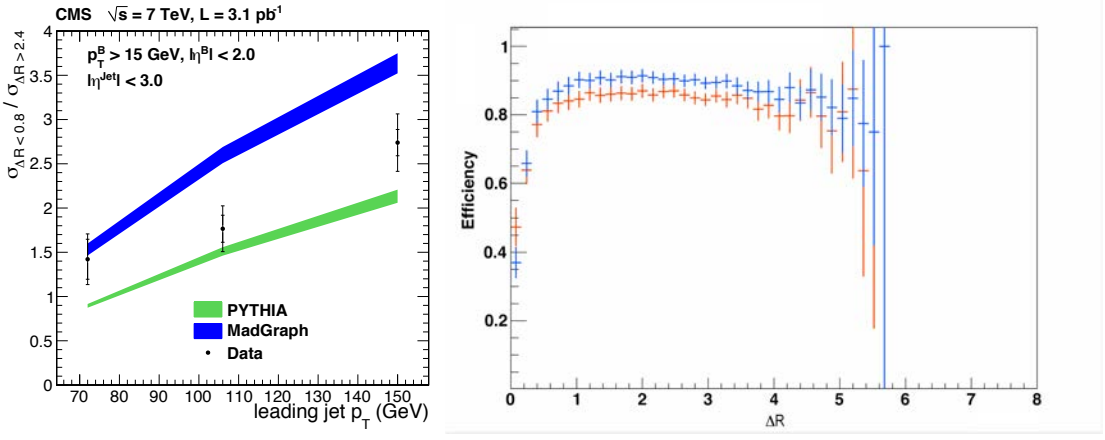


Figure 1.14: Left: Ratio between the gluon splitting region ($\Delta R$ <0.8) and the back-to-back region ($\Delta R$ >2.4) for three values of the $p_T$ cut. Right: Double vertex reconstruction efficiency as a function of $\Delta R$ for a vertex separation of 20 $\mu m$. The data are shown in red, the simulation in blue.

### 1.8 Preparations for the pixel detector upgrade

The pixel system will be replaced in 2016 – 2017 during the "Phase 1" luminosity upgrade. Major modifications to the detector layout and to the readout electronics will be needed to prevent data losses and to provide sufficiently good performance in hit and track reconstruction. The new detector will include an additional fourth barrel layer and one disk in each endcap section. The passive material will be reduced by up to a factor of two in the central tracking region, thanks to the new readout electronics and evaporative cooling technique. Adopting the 0.13 $\mu$m CMOS technology for the front-end chip in the innermost layers is currently under evaluation.

We have assessed the performance of the upgraded detector using simulation and a modified version of the detector layout [20]. Substantial improvement was observed for the track parameter resolution and vertex reconstruction performance. For the transverse impact parameter resolution the expected enhancement is about 25% in the barrel (fig.1.15, left) and up to 40% in the endcaps. The transverse primary vertex resolution for the current and upgraded detector is shown in fig.1.15 (right). The improvement is about 20%. A 20% improvement is expected on decay vertices from $b$-hadrons. A replacement of the heavily irradiated sensors in the innermost barrel layer will be required by the end of the high luminosity run. A sizeable improvement (up to 50%) in spatial resolution and track reconstruction performance was also estimated with thinner sensors with smaller pixel cells (75×100 $\mu$m$^2$).

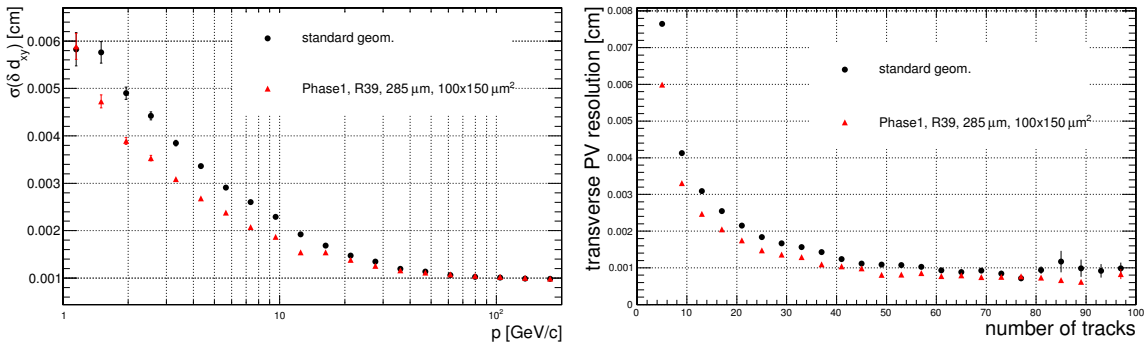


Figure 1.15: *Left: Transverse impact parameter resolution as a function of number of tracks for a luminosity of $10^{34}$ $cm^{-2}s^{-1}$. The present (black circles) and the upgraded pixel detector (red triangles) are compared. Right: Transverse primary vertex position resolution as a function of the number of tracks.*

Data taking with CMS was resumed in March 2011 at $\sqrt{s}$ = 7 TeV and will continue at least until December 2012, with a short technical stop during the 2011/12 winter holidays. The LHC luminosity in 2011 has already exceeded $3.5 \times 10^{32}$ cm$^{-2}$s$^{-1}$, surpassing the values achieved in 2010. The expected integrated luminosity for the 2011/12 period is of several fb$^{-1}$. The machine should be able to reach the design center-of-mass energy of $\sqrt{s}$ = 14 TeV after the 2013 – 2014 shut-down.

## References

[1] S. Chatrchyan *et al.* [CMS Collaboration], Journal of Instrumentation **3** (2008) S08004
[2] Y. Allkofer *et al.*, Nucl. Instr. Meth. in Phys. Research **A 584** (2008) 2
[3] V. Chiochia *et al.*, Nucl. Instr. Meth. in Phys. Research **A 568** (2006) 51

[4] A. Schmidt *et al.*, Journal of Instrumentation **4** (2009) P05003
[5] V. Khachatryan *et al.* [CMS Collaboration], JHEP **1103** (2011) 136
[6] V. Khachatryan *et al.* [CMS Collaboration], Eur. Phys. J. C **70** (2010) 1165
[7] M. Swartz, Nucl. Instrum. Meth. **A 511** (2003) 88
[8] V. Khachatryan *et al.* [CMS Collaboration], Eur. Phys. J. **C 71** (2011) 1575
[9] V. Khachatryan *et al.* [CMS Collaboration], CMS-PAS-HIG-10-002
[10] L. Wilke, PhD-Thesis, University of Zurich (2009)
[11] K. Nakamura *et al.* (Particle Data Group) J. Phys. G: Nucl. Part. Phys. **37** (2010) 075021
[12] E. Klempt and J.-M. Richard, Rev. Mod. Phys. **82** (2010) 1095
[13] W.Y.P. Hwang and D.B. Lichtenberg, Phys. Rev. **D 35** (1987) 3526
[14] T. Aaltonen et al., Phys. Rev. Lett. **99** (2007) 202001
[15] A. Schmidt, Proceedings of Science (EPS-HEP 2009) 439
[16] The CMS Collaboration, CMS Physics Analysis Summary BTV-10-001 (2010)
[17] R. Fruewirth, W. Waltenberger, and P. Vanlaer, CMS Note 2007/008 (2007)
[18] The CMS Collaboration, CMS Physics Analysis Summary BPH-10-009 (2010)
[19] CMS collaboration, submitted to J. of High Energy Phys.
[20] C. Favaro, Nucl. Instrum. Meth in Phys. Research **A** (in print)

# 2 Study of Coulomb-bound $\pi K$-pairs

C. Amsler, A. Benelli[2], C. Regenfus, and J. Rochet

*In collaboration with:*
CERN, Czech Technical University, Institute of Physics and Nuclear Physics Institute ASCR (Czech Republic), Laboratori Nazionali di Frascati, Messina University, Trieste University, KEK, Kyoto Sangyo University, Tokyo Metropolitan University, IFIN-HH (Bucharest), JINR (Dubna), Skobeltsin Institute for Nuclear Physics (Moscow), IHEP (Protvino), Santiago de Compostela University, Bern University.

(DIRAC Collaboration)

The DIRAC experiment at CERN (PS212) is measuring the lifetime of electromagnetically bound $\pi^+\pi^-$- or $\pi^\mp K^\pm$-pairs ($\pi\pi$-atoms or pionium, and $\pi K$-atoms). Results for $\pi\pi$-atoms have been published earlier by the DIRAC-I collaboration [1]. The final result for the mean life [2] is 3.15 $\pm$ 0.20 (stat) $\pm$ 0.19 (syst) fs which leads to the determination of the difference in the isospin 0 and 2 $\pi\pi$-scattering lengths with a precision of 4%, namely $|a_0 - a_2|$ = 0.2533 $\pm$ 0.0079 (stat) $\pm$0.0075 (syst) $m_\pi^{-1}$, in agreement with results obtained from $K$-decay into $3\pi$ [3] and $K$-decay into $2\pi e\nu$ [4].

We are mainly involved in the study of $\pi K$-atoms (DIRAC-II experiment) for which we developed and built the aerogel Čerenkov counters to distinguish pions from kaons. The mean life of the $\pi K$-atom is related to the isospin 1/2 and 3/2 $\pi K$ scattering lengths ($a_{1/2}$ and $a_{3/2}$) or, more precisely, to the absolute value of the difference between the two scattering lengths, a quantity that was calculated within 5% from Roy-Steiner dispersion-relations [5]. A measurement of the mean life will test low-energy QCD concepts involving the $u$- and $d$-quarks for $\pi\pi$, and extending to the $s$-quark sector for $\pi K$. The expected mean life of $\pi K$-atoms is 3.7 fs with large uncertainty [6].

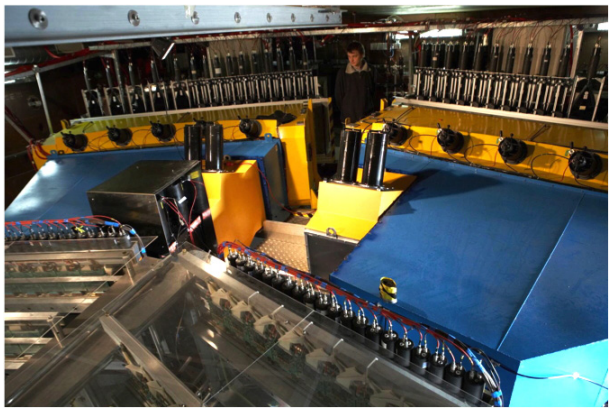

Figure 2.16: *Photograph of the DIRAC experiment showing the aerogel counters (black box on the left), the heavy gas counters (small yellow boxes) and the $N_2$ counters (blue boxes). The vertical photomultipliers at the back reject muons.*

Details on the apparatus can be found in ref. [7] and in previous annual reports. We use the 24 GeV/c proton beam from the PS which traverses a thin Pt- (or Ni-) target. The secondary particles emerging from the target in the forward direction are analyzed in a double-arm magnetic spectrometer. Electrons and positrons are vetoed by $N_2$-Čerenkov detectors and muons by scintillation counters behind thick absorbers. Kaons are separated from pions and protons by heavy gas ($C_4F_{10}$)

[2]Visitor from JINR, Dubna

Čerenkov counters (which fire on pions) and by an aerogel Čerenkov counters (which fires on both pions and kaons, but not not on the more numerous protons). Our group has developed and built the $37\ell$ aerogel Čerenkov counter [8] and the gas system for the $C_4F_{10}$ counters [9]. The aerogel detector consists of three independent modules. Two of them have refractive index $n = 1.015$ and are used for kaons between 4 and 5.5 GeV/c. At small angles with respect to the primary beam axis the momenta increases up to 8 GeV/c and hence an aerogel counter with lower refractive index ($n = 1.008$) is used to suppress fast protons. A photograph of the equipment downstream of the dipole magnet is shown in fig. 2.16

The measurement method was described in previous annual reports. Figure 2.17 shows the four mechanisms which contribute to the production of $\pi^{\pm}K^{\mp}$-pairs. Briefly, $\pi K$- (or $\pi\pi$-) atoms produced by incident protons fly in the forward direction and are ionized while crossing the target, leading to a peak from "atomic" pairs at very small relative momenta between the two particles (typically $<$ 3 MeV/c in the c.m.s system). Since ionization competes with other processes such as annihilation, the number of atomic pairs grows with increasing lifetime. Unbound $\pi K$-pairs ("Coulomb-pairs") which interact electromagnetically are also produced and their numbers are related to the number of atoms [10]. The background stems from non-Coulomb pairs due to $K$ and $\pi$ mesons from long-lived resonances (which therefore do not interact), and from accidentals (pairs produced by two different proton interactions).

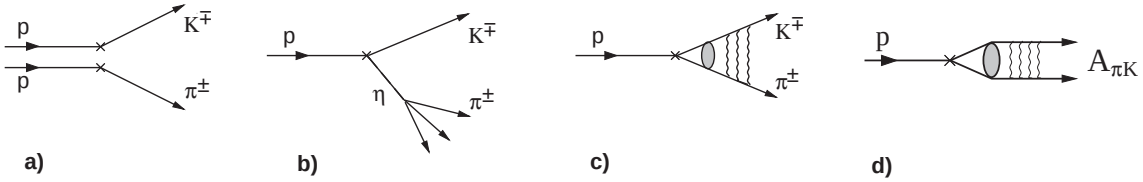


Figure 2.17: *Production mechanisms of $\pi K$-pairs: a) accidental-pairs from two protons; b) non-Coulomb-pairs from long-lived intermediate states such as the $\eta$-meson; c) Coulomb-pairs from direct production or from short-lived intermediate states; d) $\pi K$-atoms.*

The DIRAC collaboration observed $\pi K$-atoms for the first time with the data collected in 2007 [11]. This result led to a lower limit for the mean life of $\pi K$-atoms of 0.8 fs in the $1s$-state, which could be translated into an upper limit of $|a_{1/2} - a_{3/2}| < 0.58\ m_{\pi}^{-1}$. Details can be found in ref. [11, 12, 13].

For the 2007 data we had used only the detectors downstream of the magnet. Three main improvements were implemented for the 2008 – 2010 runs. A scintillation fibre detector (SFD, described below) and microdrift chambers are now available to determine the interaction point in the production target with better precision. The SFD measures tracks with good resolution ($\sigma$ = 60 $\mu$m), high efficiency (98%) and improves the resolution on the transverse momentum $Q_T$ from 3 MeV/c to 1 MeV/c, which reduces the background by typically a factor of four. ADC's for the aerogel detectors were also not available in the 2007 runs while this information is now recorded and, accordingly, the detection efficiency for kaons with the aerogel and the contamination from protons can be calculated reliably. The detection efficiency for kaons is typically 95% above 5 GeV/c and the contamination from protons around 5%, except for high energy protons close to the beam axis for which the proton contamination rises significantly. However, simulation shows that even a contamination of 100% is not problematic since no enhancement is observed for protons at small relative longitudinal momenta.

Finally, in 2007 the main goal was the observation of $\pi K$-atoms and hence a platinum target was chosen for which the production cross section was high. However, for platinum the breakup probability as a function of mean life (53% for 3.7 fs) is flattening off above $\sim$ 4 fs and hence we

could only give a lower limit for the mean life. We now use a nickel target for which the dependence between breakup probability and mean life is described by a steeper function, although atoms are produced with a lower cross section.

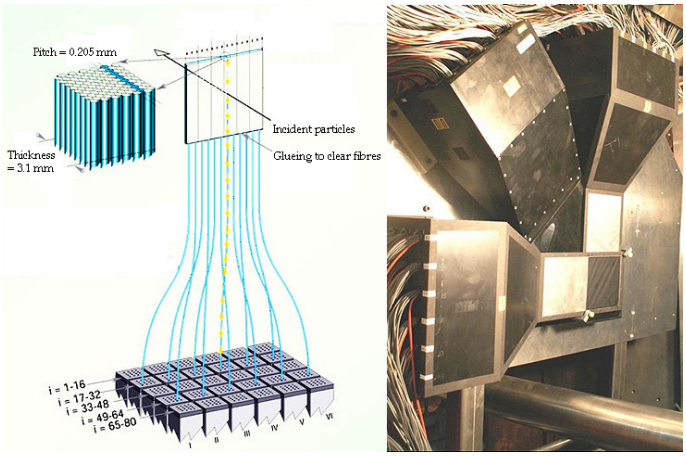


Figure 2.18: *Layout of the scintillating fibre detector and photograph showing the three detection planes.*

During 2010 we tuned the Monte Carlo simulation of the scintillation fibre detector (SFD). A sketch of the detector is shown in fig. 2.18 (left). The detector consists of 3 planes ($x$, $y$, and $w$) of scintillating fibres (diameter 205 $\mu$m). The $x$- and $y$-planes are made of 8 layers each with 480 fibres while the $w$-planes contain 3 layers of 320 fibres. The fibres are read out in columns of 8, respectively 3 fibres by 30 $\times$ 16 Hamamatsu H6568 photomultipliers. The area covered by each plane is about 10 $\times$ 10 cm$^2$ and contributes only 1% radiation length. The timing resolution is 460 ps. A photograph of the detector is shown in fig. 2.18 (right).

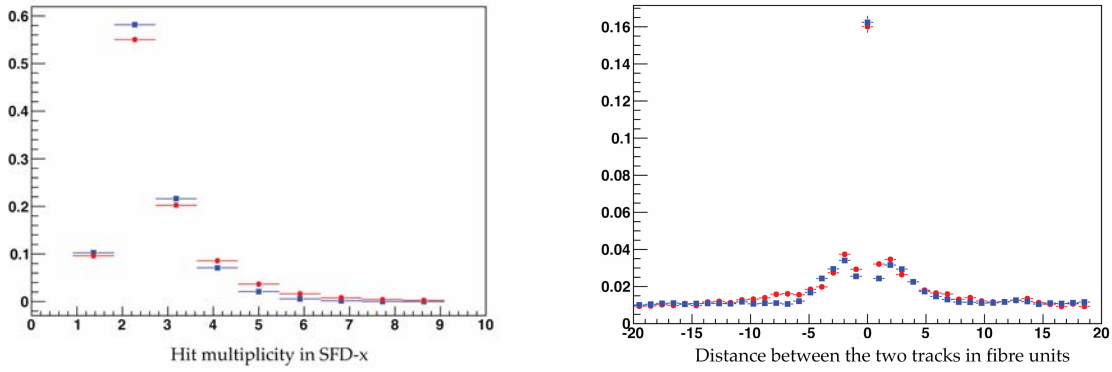


Figure 2.19: *Left: Hit multiplicity distribution in the SFD x plane after the peak sensing algorithm. Right: Distribution of the distance between the $\pi^+$ and $\pi^-$ tracks in the $x$-plane of the SFD. The data are shown in red, the simulation in blue.*

We now illustrate the performance of the SFD using $\pi^+\pi^-$ data which are more abundant than $\pi K$ data. The $x$-plane of the SFD detector was equipped with new readout electronics featuring both TDC's and ADC's. An important software tool was developed using the ADC information, the peak sensing algorithm, which compares the signal amplitudes for neighbouring hits to reduce

background. Figure 2.19 (left) compares the measured hit multiplicity with simulation after having applied the peak sensing algorithm. Figure 2.19 (right) shows the distribution of the distance between two tracks measured by the SFD $x$-plane. In both plots good agreement between data and simulation is observed.

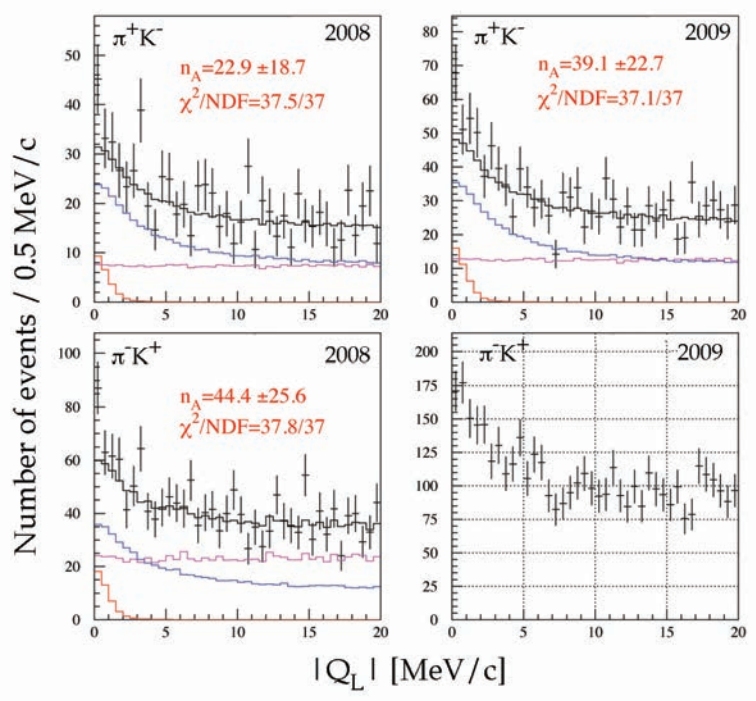


Figure 2.20: *Top: Distribution of longitudinal relative momenta $Q_L$ for $\pi^+K^-$-events for the 2008 and 2009 data. Bottom: Distribution for $\pi^-K^+$-events. The data are shown by the points with error bars, the histograms are described in the text. The 2009 analysis of the $\pi^-K^+$ signal is in progress.*

In 2010 we also proceeded with the analysis of the 2008 –2009 data with the upstream detectors, selecting $\pi K$ events as cleanly as possible. The SFD detector and the nearby ionization hodoscope are used to resolve double tracks. Drift chamber (DC) tracking is performed and only upstream tracks that have hits in the SFD are kept. The distance between the DC extrapolation at the SFD plane and the actual SFD hit has to be smaller than 1 cm. Particle identification using the heavy gas Cerenkov and aereogel detectors is then performed and a precise timing between the two tracks is required. The relative transverse momentum is required to be smaller than $Q_T = 4$ MeV/c, the relative longitudinal momentum less than $|Q_L| = 20$ MeV/c.

Figure 2.20 (top) shows superimposed the experimental distribution of $\pi^-K^+$ (points with error bars) with the result of the fit containing atomic pairs (red line), Coulomb pairs (blue line) and non-Coulomb pairs (magenta line). The sum of Coulomb and non-Coulomb pairs is shown by the black line. The analysis of the corresponding $\pi^-K^+$-events is shown in fig. 2.20 (bottom).

A method to measure the energy difference $\Delta E_n$ between the pionium $np$- and $ns$-states was proposed as follows [14]. When moving inside the target, the atoms interact with an applied electric field. Some of them leave the target in the $2p$-state. The decay into $\pi^0\pi^0$ being forbidden from $p$-states the main decay process is $2p - 1s$ radiative transition with subsequent annihilation from $1s$ into $\pi^0\pi^0$. Thus, the mean life of the atom in the $2p$-state is determined by radiative transition, $\tau(2p) \simeq 12$ ps [10], which is much slower than annihilation from $ns$-states. One can then measure

the energy difference $\Delta E_n$ by observing the field dependence of the decay rate in the applied electric field. This determines the combination $2a_0 + a_2$ of the $\pi\pi$-scattering lengths. Combining with our measurement from the $1s$-state we will be able to derive $a_0$ and $a_2$ separately. This method can also be applied to the $\pi K$-system to obtain $a_{1/2}$ and $a_{3/2}$ separately.

During summer 2010 DIRAC took data with excellent detector performance and stable beam from the PS accelerator. DIRAC has been approved to run at least until the end of 2011. More data on $\pi K$-atoms will be collected in 2011 together with measurements of the energy difference between the $ns$ and $np$ states of pionium.

## References

[1] B. Adeva *et al.* (DIRAC Collaboration), Phys. Lett. **B 619** (2005) 50
[2] B. Adeva *et al.* (DIRAC Collaboration), submitted to Phys. Rev. Lett.
[3] J. R. Bately *et al.*, Eur. Phys. J. **C 64** (2009) 589
[4] J. R. Bately *et al.*, Eur. Phys. J. **C 70** (2010) 635
[5] P. Büttiker, S. Descotes-Genon, B. Moussallam, Eur. Phys. J. **C 33** (2004) 409
[6] J. Schweizer, Phys. Lett. **B 587** (2004) 33
[7] B. Adeva *et al.* (DIRAC Collaboration), Nucl. Instrum. Methods in Phys. Res. **A 515** (2003) 467
[8] Y. Allkofer *et al.*, Nucl. Instr. Meth. in Phys. Res. **A 582** (2007) 497;
Y. Allkofer *et al.*, Nucl. Instr. Meth. in Phys. Res. **A 595** (2008) 84
[9] S. Horikawa *et al.*, Nucl. Instr. Meth. in Phys. Res. **A 595** (2008) 212
[10] L. L. Nemenov, Sov. J. Nucl. Phys. **41** (1985) 629;
L. Afanasyev and O. Voskresenskaya, Phys. Lett. **B 453** (1999) 302
[11] B. Adeva *et al.* (DIRAC Collaboration), Phys. Lett. **B 674** (2009) 11
[12] Y. Allkofer, PhD Thesis, University of Zurich (2008)
[13] C. Amsler, Proc. of Science PoS EPS-HEP (2009) 078
[14] Addendum to PS212 (09/02/11): CERN-SPSC-2011-001 (SPSC-P-284 Add. 5)

# 3 Towards a dark matter experiment

Y. Allkofer, C. Amsler, V. Boccone, W. Creus, A. Ferella, P. Otyugova, C. Regenfus, L. Scotto Lavina, J. Rochet, and M. Walter[3]

*Together with* the ArDM and the DARWIN Collaborations

The interaction of Weak Interacting Massive Particles (WIMPs) with nuclei in a dark matter detector generates recoil energies below typically 100 keV. The differential cross section decreases exponentially with increasing recoil energy. This makes WIMP detection difficult due to the low energy background. Hence massive detectors with low detection thresholds are needed, among them cryogenic ones using noble liquids such as liquid argon (LAr). The Zurich group has designed and built the light readout system for the 1 ton LAr detector ArDM which is being developed at CERN. Details on the detector can be found in previous annual reports and in recent publications [1, 2, 3, 4].

The ArDM detector was filled for the first time with 1 ton of LAr in 2009. Several important parameters such as stable cryogenic operation in high LAr purity, high scintillation light yield, and detection of events down to energies of tens of keV's could be verified. The test was performed with a partial light readout assembly consisting of half of the PMT's[4], no electric field and no charge readout. The LAr purity was found to be constant over the measurement time of three weeks by monitoring the decay time of the slow component of the light signal [3].

The measurements were done with external sources such as $^{22}$Na, delivering positrons (annihilating into two 511 keV $\gamma$'s) and monochromatic 1275 keV $\gamma$'s. The light yield produced by one of the 511 keV $\gamma$'s, following (multiple) Compton scattering, was measured by triggering with a 4" Na(Tl) crystal on the second 511 keV emitted in the opposite direction, and on the 1275 keV $\gamma$. Figure 3.21 shows the light yield distributions for the source located at two different vertical distances from the photomultiplier array (black bars) [3]. The light yield (in photoelectrons, p.e.) was calculated by Monte Carlo simulation as a function of energy deposit, and the distributions (red bars) compared to the measured ones. Good agreement is found with an average light yield of typically 0.4 p.e./keV, which is roughly half of the yield that would be obtained with a completed detector (14 PMT's)[5]. We are therefore confident to be able to reach our goal of 30 keV threshold in ArDM for WIMP detection.

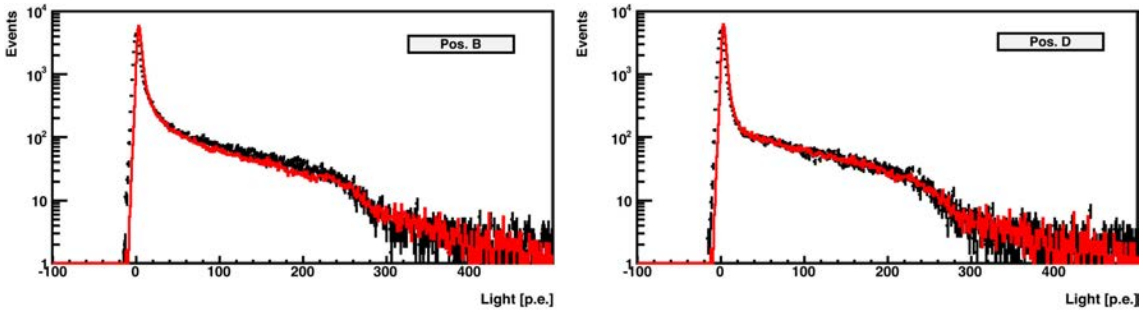


Figure 3.21: *Light yield in the 1-ton LAr detector for 511 keV $\gamma$'s (in photoelectrons, p.e.) at two positions of the $^{22}$Na- source. The measurements are in black, the simulated data in red.*

[3] Diploma student from Universität Konstanz

[4] 7 Hamamatsu R5912-MOD 8" PMT's with Pt-underlay

[5] Note that the light yield for nuclear recoils is lower due to quenching, typically 30% of that for electrons in the few 10 keV range, see fig. 3.26 below.

The light yields of nuclear recoils in LAr are poorly known, especially below 50 keV (see e.g. ref. [5]). A suitable way to produce nuclear recoils of known energies in the lab is $n$-Ar elastic scattering with monoenergetic neutrons, detecting the neutron as a function of scattering angle. We have therefore set up a scattering experiment with collimated 2.45 MeV neutrons from our $dd \rightarrow {}^3$He $n$ source [6]. The target is a small ($<1\ell$) test cell (77 mm high and 74 mm in diameter) and liquid scintillation counters (LSC, EJ301 from SCIONIX) detect the scattered neutrons in coincidence as a function of scattering angle (fig. 3.22). To reduce the measurement time we use four LSC's to cover various angles in parallel (fig. 3.22).

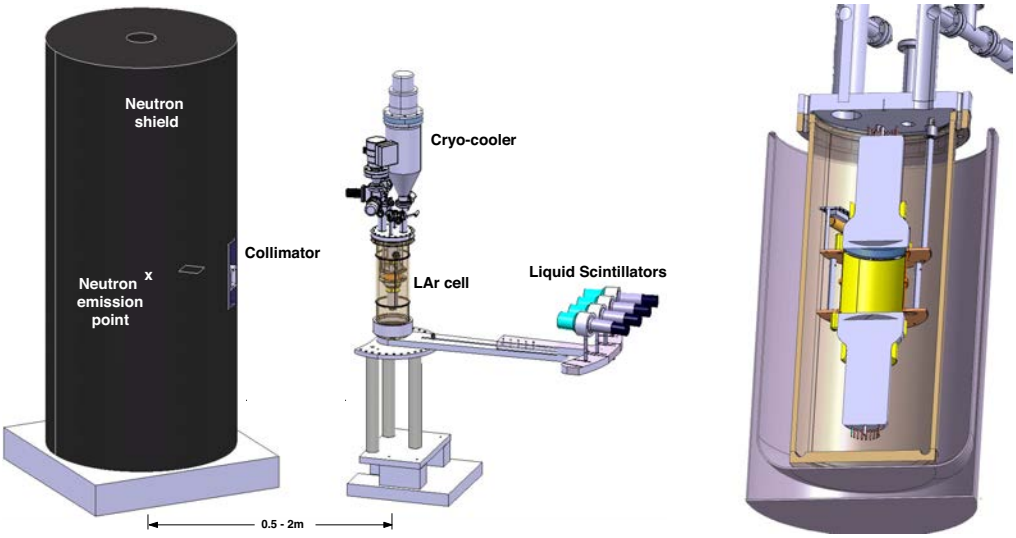


Figure 3.22: *Left: Sketch of the neutron generator with polyester shielding (black cylinder), the LAr cell, the cryocooler and the four liquid scintillators (LSC) to detect the scattered neutrons. The right picture shows the LAr cell with its 2 PMT's on top and bottom of the LAr volume.*

The fusion chamber is surrounded by a 90 cm diameter shield of borated polyester and the experiment confined within a radiation controlled fence in our laboratory at CERN. Residual radiation (mainly from scattered neutrons and X-rays) is well below the authorized limit of 2.5 $\mu$Sv/h. The neutrons are collimated through a polyethylene orifice within roughly $1\% \times 4\pi$ sr. The neutron flux (up to $5\times10^6$ n/s in $4\pi$ according to specifications) is controlled through the applied high voltage and discharge current.

The neutron flux was measured with a 5" LSC located at the collimator exit. The polyethylene collimator was surrounded by a 2 mm thick lead box against X-rays inserted into the polyester shielding. According to NSD-Fusion, the highest possible voltage and current are 100 kV, resp. 15 mA, corresponding to a flux of $10^7$n/s into $4\pi$. The flux increases proportionally to the current and to the voltage $V^{2.8}$. Measurements were made with and without polyethylene collimator and the rates corrected for the solid angle, assuming a detection efficiency of the LSC of 80%. A NIM MPD-4 module was used to discriminate between neutrons and X-rays. Figure 3.23 shows the measured neutron intensity (blue, red and orange points) compared with the values specified by NSD-Fusion (green crosses for 10mA and orange crosses for 15mA [6]). Insufficient lead shielding leads to a strong X-ray contamination. The measured flux was roughly one order magnitude smaller than anticipated, with a maximum of $10^6$ n/s. However, the generator was upgraded recently by NSD-fusion, leading to a factor 2 – 3 improvement in neutron flux.

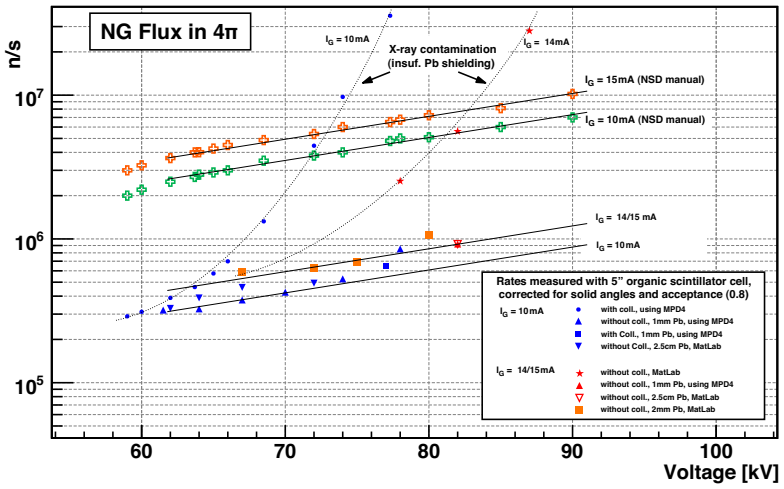


Figure 3.23: *Neutron generator flux into 4π (see text). Straight lines are drawn to guide the eye.*

The neutron energy distribution (smeared by collimator scattering) must be known to measure the light yield from LAr accurately. Figure 3.24 (left) shows the neutron energy distribution measured by a 5" LSC placed at the exit of the collimator. Ideally the spectrum should be flat without collimator scattering, infinite resolution and single $n$-scattering. The spectrum of fig. 3.24 (right) was obtained by unfolding the response of the LSC to neutrons from a radioactive source. The latter was obtained with an AmBe-source, by measuring the neutron energy through the time-of-flight between the source and the neutron counter over a distance of 1 m. The start time was determined from the 4.4 MeV $\gamma$ detected in a BGO crystal located close to the AmBe-source.

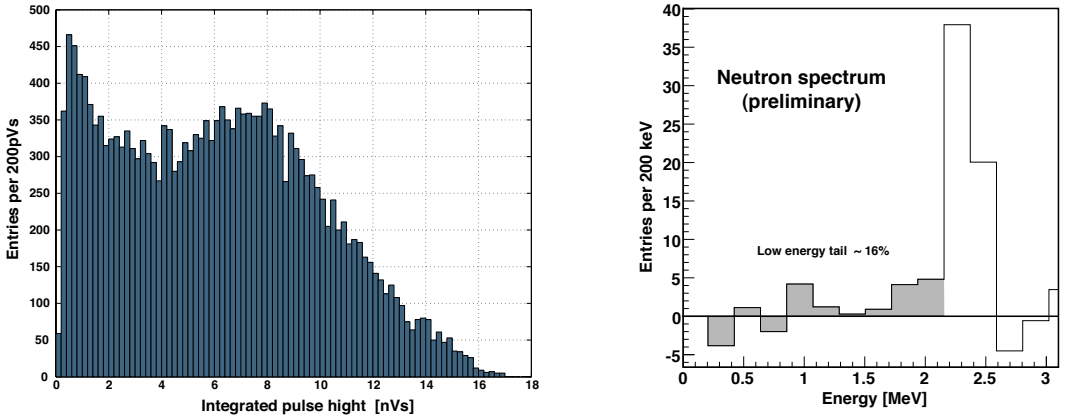


Figure 3.24: *Left: Signal spectrum of neutrons in the LSC at the exit of the collimator. Right: Energy spectrum obtained after unfolding the response of the LSC.*

We have started to measure the scintillation response of LAr to nuclear recoils with the LAr cell shown in fig. 3.22 (right). Wavelength shifting reflectors (Tetraphenyl-Butadiene, TPB, on Tyvek foils) were mounted on the inner walls of the cell to convert the 128 nm light into 400 nm. The cell was read out by two Hamamatsu R6091-01MOD PMT's with platinum underlay for cryogenic operation. An internal $^{210}$Pb-source emitted 5.3 MeV $\alpha$'s and up to 1.2 MeV electrons. The component ratio $CR$

is defined as the ratio of integrated light yield during the first 50 ns to the total light yield. Thus a high $CR$ corresponds to the emission of light with mainly the fast component. Heavily ionizing particles such as $\alpha$'s or nuclear recoils lead to a large $CR$ value [7]. Figure 3.25 shows the component ratio $CR$ from one of our first measurements of argon luminescence with the fusion generator. A clear contribution from neutron induced nuclear recoils is observed at $CR \sim 0.8$.

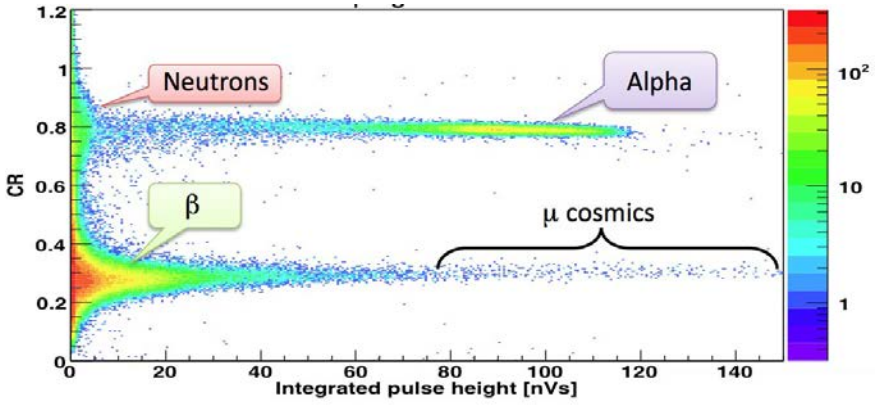


Figure 3.25: *Component ratio $CR$ in LAr for 2.45 MeV neutrons, 5.3 MeV $\alpha$'s and 1.3 MeV electrons and cosmic muons.*

A first measurement of the scintillation efficiency for nuclear recoils relative to electrons was performed with a 5" LSC at $65°$ from the incident beam direction, at a distance of 50 cm from the LAr cell. The time-of-flight between the LAr cell and the LSC's could be determined off-line and used to remove background, e.g. from multiple neutron scattering in the cell. The reference time was determined with a Na-source located at equal distance from the LAr-cell and the LSC, and using the two back-to-back 511 keV $\gamma$'s. At $65°$ the argon recoil energy is 69 keV with 2.45 MeV incident neutrons. This corresponds to a time-of-flight of 23 ns for 2.4 MeV neutrons flying to the LSC. Good pulse shape separation between proton and background ($\gamma$-induced electron recoils) could be achieved with the LSC by analogue pulse shape discrimination.

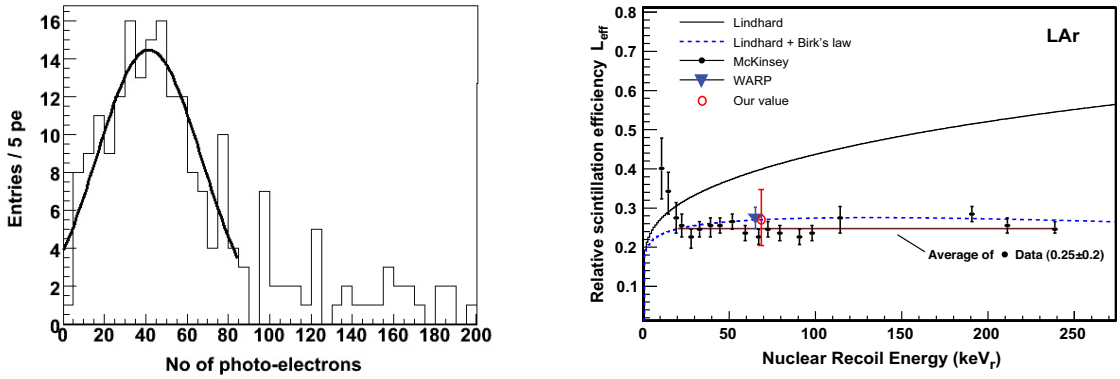


Figure 3.26: *Left: Integrated pulse height distribution in the LAr cell for neutron scattering at $65°$. Right: Measurement of the relative scintillation efficiency in LAr as a function of recoil energy (from ref. [5]). Our preliminary measurement is shown by the red data point.*

Several cuts were applied in the offline analysis. For example, we required the component ratio

$CR$ to be larger than 0.6 (see fig. 3.25). We also rejected events close to the PMT windows by comparing the signals from the two PMT's. A time-of-flight window between 18 and 31 ns was selected. Figure 3.26 (left) shows the pulse height distribution in LAr for 69 keV recoils. We obtained a scintillation efficiency of 0.27 (with about 25% error) in this first attempt. Figure 3.26 (right) shows our data point compared with data from ref. [5].

Light yields of nuclear recoils are usually determined relative to electronic recoils. The electronic light yield is determined with various external $\gamma$-sources and also with a $^{83}\mathrm{Kr}^{m}$ source which can be connected directly to the gaseous phase in our setup. We use a linear dependence on energy between 60 and 1062 keV, but are working on a calibration at the 122 keV line from $^{57}$Co, as is the standard in the field. To improve the light yield and the measurements with radioactive sources we upgraded our LAr cell to reduce the thickness of the stainless steel vessel and the LAr volume. Tetratex foils[6] were used instead of the Tyvek reflectors, and TPB-Paraloid coating was replaced by 0.08 mg·cm$^{-2}$ of evaporated TPB. Figure 3.27 shows the spectrum of the 60 keV line from Am-decay. During data taking the mean life of the the slow component was much lower than the established value of 1.6 $\mu$s, due to the impurity of the LAr (see e.g. ref. [3]). By extrapolating the light yield to maximum purity we could set a lower limit of 3.2 p.e./keV.

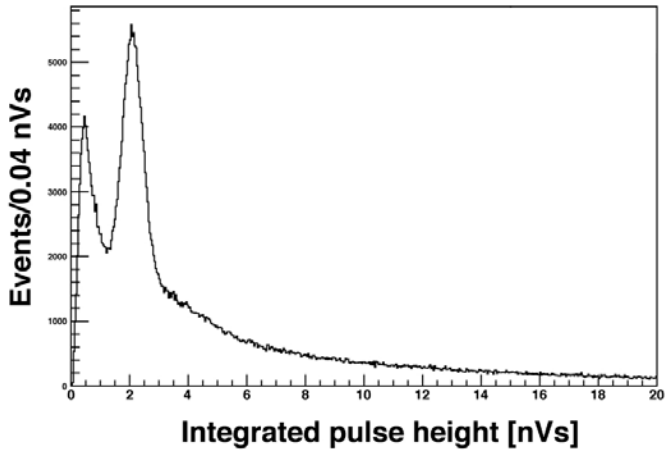


Figure 3.27: Energy spectrum from Am-decay measured with the refurbished LAr cell, showing the 60 keV line.

Most of the mechanical components for the final measurements are now installed in our laboratory. During the next months we will commission the gas handling system and the cryocooler (Gifford-McMahon-type) mounted on top of the LAr cell. A cooling serpentine is bonded to the temperature regulated cold head and provides the liquefaction of the recirculated gas. Gas purification is achieved by two cleaning cartridges. They reduce the $O_2$ and $H_2O$ contamination in the gas below 20 ppm. A second air blower has been installed for the neutron generator to operate at maximum power. The completed system will be operational by summer 2011, ready for data taking during several weeks to accumulate enough statistics at various scattering angles. A further upgrade of the LAr cell with a smaller active volume (and less surrounding material) to reduce multiple scattering and enhance the light yield is also foreseen.

## References

[1] C. Amsler *et al.*, Journal of Instrumentation **3** (2008) P02001
[2] V. Boccone *et al.*, Journal of Instrumentation **4** (2009) P06001

[6] From Donaldson Membranes

[3] C. Amsler *et al.*, Journal of Instrumentation **5** (2010) P11003
[4] V. Boccone, PhD-Thesis, Universität Zürich, 2010
[5] D. Gastler *et al.*, arXiv:1004.0373v1 [physics.ins-det]
[6] NSD-Fusion: http://www.nsd-fusion.com
[7] A. Hitachi *et al.*, Phys. Rev. **B 27** (1983) 5279

# 4 Publications

### Articles

1. First results on the light readout from the 1-ton ArDM liquid argon detector for dark matter searches
   C. Amsler et al. (ArDM Collaboration)
   Journal of Instrumentation **5** (2010) P11003

2. Review of Particle Physics
   K. Nakamura et al. (Particle Data Group)
   Journal of Physics **G 37** (2010) 075021

3. Particle Physics Booklet
   K. Nakamura et al. (Particle Data Group)
   IOP Publishing, 2010

4. Note on scalar mesons
   C. Amsler, T. Gutsche, S. Spanier and N.A. Törnqvist
   Journal of Physics G: Nucl. and Part. Phys. **37** (2010) 075021-680

5. The $\eta(1405)$, $\eta(1475)$, $f_1(1420)$, and $f_1(1510)$
   C. Amsler and A. Masoni
   Journal of Physics G: Nucl. and Part. Phys. **37** (2010) 075021-630

6. Quark Model
   C. Amsler, T. DeGrand and B. Krusche
   Journal of Physics G: Nucl. and Part. Phys. **37** (2010) 075021-184

7. Test in liquid argon of the light readout system for the ArDM experiment
   V. Boccone
   IEEE Nucl. Science Symp. Conf. Rec., Orlando **N25**-153 (2009)

8. Development and test in liquid argon of the light readout system for the ArDM experiment
   V. Boccone
   AIP Conf. Proc. Volume **1182** (2009) 280

9. The ArDM-a ton-scale liquid argon experiment for direct Dark Matter Detection
   P. Otyugova
   Invisible Universe: Proceedings of the Conference
   AIP Conf. Proc., Volume **1241** (2010) 435

10. The ArDM-a ton-scale liquid argon experiment for direct Dark Matter Detection
    P. Otyugova
    Proc. 5th Patras Workshop on Axions, WIMPs and WISPs, Durham, UK
    DESY-PROC-2009-05

11. The Argon Dark Matter Experiment
    C. Regenfus
    Proceedings of the TAUP 2009 Conference, Rome
    J. Phys. Conf. Ser. **203** (2010) 012024

12. Study of the Bs meson with forthcoming LHC data at CMS
B. Millán Mejías
VIII Latin American Symposium on Nuclear Physics and Applications
AIP Conf. Proc. Volume **1265** (2010) 264

13. Beam Background Effects in the CMS Pixel Detector
H. Snoek
Proc. of Science (Vertex 2010 - 013)

14. First measurements of beauty quark production at $\sqrt{s} = 7$ TeV with the CMS experiment
V. Chiochia
Nuclear Physics **A 855** (2011) 436

15. Supersymmetry with Multijet Events at CMS: an Experimental Strategy
T. Rommerskirchen
Inaugural Dissertation, Universität Zürich, 2010

16. Light Readout for a 1 ton Liquid Argon Dark Matter Detector
V. Boccone
Inaugural Dissertation, Universität Zürich, 2010

17. Search for Quark Compositeness with the Dijet Centrality Ratio in $pp$ Collisions at $\sqrt{s} = 7$ TeV
CMS Collaboration
Phys. Rev. Lett. **105** (2010) 262001

18. Search for Dijet Resonances in 7 TeV pp Collisions at CMS
CMS Collaboration
Phys. Rev. Lett. **105** (2010) 211801

19. Observation of Long-Range Near-Side Angular Correlations in Proton-Proton Collisions at the LHC
CMS Collaboration
J. High Energy Physics **1009** (2010) 091

20. CMS Tracking Performance Results from early LHC Operation
CMS Collaboration
Eur. Phys. J. **C 70** (2010) 1165

21. First Measurement of the Underlying Event Activity at the LHC with $\sqrt{s} = 0.9$ TeV
CMS Collaboration
Eur. Phys. J. **C 70** (2010) 555

22. Measurement of the charge ratio of atmospheric muons with the CMS detector
CMS Collaboration
Phys. Lett. **B 692** (2010) 83

23. Transverse-momentum and pseudorapidity distributions of charged hadrons in $pp$ collisions at $\sqrt{s} = 7$ TeV
CMS Collaboration
Phys. Rev. Lett. **105** (2010) 022002

24. First Measurement of Bose-Einstein Correlations in proton-proton Collisions at $\sqrt{s}$ = 0.9 and 2.36 TeV at the LHC
CMS Collaboration
Phys. Rev. Lett. **105** (2010) 032001

25. Transverse momentum and pseudorapidity distributions of charged hadrons in $pp$ collisions at $\sqrt{s}$ = 0.9 and 2.36 TeV
CMS Collaboration
J. High Energy Physics **1002** (2010) 041

26. Measurement of the muon stopping power in lead tungstate CMS Collaboration
J. Instrumentation **5** (2010) P03007

27. Measurement of $B\bar{B}$ Angular Correlations based on Secondary Vertex Reconstruction at $\sqrt{s} =$ 7 TeV
CMS Collaboration
J. High Energy Physics **1103** (2011) 136

28. Dijet Azimuthal Decorrelations in $pp$ Collisions at $\sqrt{s} = 7$ TeV
CMS Collaboration
Phys. Rev. Lett. **106** (2011) 122003

29. Search for Supersymmetry in $pp$ Collisions at 7 TeV in Events with Jets and Missing Transverse Energy
CMS Collaboration
Phys. Lett. **B 698** (2011) 196

30. Measurement of the $B^+$ Production Cross Section in pp Collisions at $\sqrt{s} = 7$ TeV
CMS Collaboration
Phys. Rev. Lett. **106** (2011) 112001

31. Search for a heavy gauge boson $W'$ in the final state with an electron and large missing transverse energy in $pp$ collisions at $\sqrt{s} = 7$ TeV
CMS Collaboration
Phys. Lett. **B 698** (2011) 21

32. Search for Microscopic Black Hole Signatures at the Large Hadron Collider
CMS Collaboration
Phys. Lett. **B 697** (2011) 434

33. Measurements of Inclusive W and Z Cross Sections in $pp$ Collisions at $\sqrt{s} = 7$ TeV
CMS Collaboration
J. High Energy Physics **1101** (2011) 080

34. Measurement of the Isolated Prompt Photon Production Cross Section in $pp$ Collisions at $\sqrt{s} =$ 7 TeV
CMS Collaboration
Phys. Rev. Lett. **106** (2011) 082001

35. Search for Stopped Gluinos in $pp$ collisions at $\sqrt{s} = 7$ TeV
CMS Collaboration
Phys. Rev. Lett. **106** (2011) 011801

36. Charged particle multiplicities in $pp$ interactions at $\sqrt{s}$ = 0.9, 2.36, and 7 TeV
CMS Collaboration
J. High Energy Physics **1101** (2011) 079

37. First Measurement of the Cross Section for Top-Quark Pair Production in Proton-Proton Collisions at $\sqrt{s} = 7$ TeV
CMS Collaboration
Phys. Lett. **B 695** (2011) 424

38. Inclusive b-hadron production cross section with muons in $pp$ collisions at $\sqrt{s} = 7$ TeV
CMS Collaboration
J. High Energy Physics **1103** (2011) 090

39. Search for Heavy Stable Charged Particles in $pp$ collisions at $\sqrt{s} = 7$ TeV
CMS Collaboration
J. High Energy Physics **1103** (2011) 024

40. Prompt and non-prompt J/psi production in $pp$ collisions at $\sqrt{s} = 7$ TeV
CMS Collaboration
Eur. Phys. J. **C 71** (2011) 1575

**Articles in press**

1. Search for Large Extra Dimensions in the Diphoton Final State at the Large Hadron Collider
CMS Collaboration
J. High Energy Phys. [arXiv:1103.4279]

2. Measurement of the lepton charge asymmetry in inclusive $W$ production in pp collisions at $\sqrt{s} = 7$ TeV
CMS Collaboration
J. High Energy Phys. [arXiv:1103.3470]

3. Search for Physics Beyond the Standard Model in Opposite-Sign Dilepton Events at $\sqrt{s} = 7$ TeV
CMS Collaboration
J. High Energy Phys. [arXiv:1103.1348]

4. Search for Resonances in the Dilepton Mass Distribution in $pp$ Collisions at $\sqrt{s} = 7$ TeV
CMS Collaboration
J. High Energy Phys. [arXiv:1103.0981]

5. Search for Supersymmetry in $pp$ Collisions at $\sqrt{s} = 7$ TeV in Events with Two Photons and Missing Transverse Energy
CMS Collaboration
Preprint [arXiv:1103.0953]

6. Search for a $W'$ boson decaying to a muon and a neutrino in $pp$ collisions at $\sqrt{s} = 7$ TeV
CMS Collaboration
Preprint [arXiv:1103.0030]

7. Study of $Z$ boson production in PbPb collisions at $\sqrt{s_{NN}}$= 2.76 TeV
CMS Collaboration
Phys. Rev. Lett. [arXiv:1102.5435]

8. Measurement of $W^+W^-$ Production and Search for the Higgs Boson in $pp$ Collisions at $\sqrt{s} =$ 7 TeV
CMS Collaboration
Phys. Lett. B [arXiv:1102.5429]

9. Search for a Heavy Bottom-like Quark in $pp$ Collisions at $\sqrt{s} = 7$ TeV
CMS Collaboration
Preprint [arXiv:1102.4746]

10. Strange Particle Production in $pp$ Collisions at $\sqrt{s} = 0.9$ and 7 TeV
CMS Collaboration
Preprint [arXiv:1102.4282]

11. Measurement of Dijet Angular Distributions and Search for Quark Compositeness in $pp$ Collisions at $\sqrt{s} = 7$ TeV
CMS Collaboration
Phys. Rev. Lett. [arXiv:1102.2020]

12. Observation and studies of jet quenching in PbPb collisions at nucleon-nucleon center-of-mass energy = 2.76 TeV
CMS Collaboration
Preprint [arXiv:1102.1957]

13. First Measurement of Hadronic Event Shapes in $pp$ Collisions at $\sqrt{s} = 7$ TeV
CMS Collaboration
Phys. Lett. B [arXiv:1102.0068]

14. Measurement of Bose-Einstein Correlations in pp Collisions at $\sqrt{s} = 0.9$ and 7 TeV
CMS Collaboration
J. High Energy Phys. [arXiv:1101.3518]

15. A new CMS pixel detector for the LHC luminosity upgrade
C. Favaro
Nucl. Instr. Meth. A, [arXiv:1104.1288]

16. Measurement of the Inclusive Upsilon production cross section in $pp$ collisions at $\sqrt{s} = 7$ TeV
CMS Collaboration
Phys. Rev. D [arXiv:1012.5545]

17. Search for Pair Production of Second-Generation Scalar Leptoquarks in $pp$ Collisions at $\sqrt{s} =$ 7 TeV
CMS Collaboration
Phys. Rev. Lett. [arXiv:1012.4033]

18. Search for Pair Production of First-Generation Scalar Leptoquarks in $pp$ Collisions at $\sqrt{s} = 7$ TeV
CMS Collaboration
Phys. Rev. Lett. [arXiv:1012.4033]

19. ArDM: a ton-scale LAr detector for direct Dark Matter searches
A. Marchionni *et al.* (ArDM Collaboration)
Proc. 1st Int. Workshop towards the Giant Liquid Argon Charge Imaging Exp. (GLA2010),

Tsukuba, Japan
arXiv:1012.5967v1 [physics.ins-det]

**Lectures**

1. E. Aguiló
   12th Topical Seminar on Innovative Particle and Radiation Detectors, Siena, Italy
   8 June 2010
   "The alignment of the CMS Silicon Tracker"

2. Y. Allkofer
   Workshop on Antimatter Physics, Bergen, Norway
   22 February 2011
   "Central Detector: boundary conditions"

3. C. Amsler
   Workshop on Antimatter Physics, Bergen, Norway
   22 February 2011
   "A hybrid detector for antigravity measurements"

4. C. Amsler
   WIN11– 23rd Int. Workshop on Weak Interactions and Neutrinos, Cape Town, South Africa
   31 January 2011
   "Search for WIMPS in liquid argon"

5. C. Amsler
   Café Scientifique, University of Fribourg, Switzerland
   17 February 2011
   "La Recherche au CERN"

6. V. Chiochia
   Workshop on Heavy Particles at the LHC, ETH Zurich
   6 January 2011
   "Beauty quark production with the CMS experiment"

7. V. Chiochia
   CERN Physics Days: Charm and Bottom Quark Production at the LHC, CERN
   3 December 2010
   "Beauty and charm production with the CMS experiment"

8. V. Chiochia
   4th Int. Conf. on Hard and Electromagnetic Probes of High-Energy Nucl. Coll., Eilat, Israel
   10 October 2010
   "Measurement of the inclusive beauty production with the CMS experiment"

9. V. Chiochia
   CMS Tracker Week, La Biodola, Isola d'Elba, Italy
   25 May 2010
   "Tracker for $b$-cross section measurements"

10. W. Creus
    Annual meeting of the Swiss Physical Society, Basel, Switzerland
    22 June 2010
    "Light yield from nuclear recoils in liquid argon"

11. S. de Visscher
    Annual meeting of the Swiss Physical Society, Basel, Switzerland
    21 June 2010
    "First results from the CMS experiment"

12. S. de Visscher
    12th Topical Seminar on Innovative Particle and Radiation Detectors, Siena, Italy
    8 June
    "Evaluation of the CMS pixel detector data from the first LHC collisions"

13. C. Favaro
    8th Int. Conf. on Rad. Effects on Semiconductor Materials Detectors and Devices, Florence
    12 October 2010
    "The upgrade of the CMS Pixel Detector"

14. C. Favaro
    Annual meeting of the Swiss Physical Society, Basel, Switzerland
    21 June 2010
    "Hit resolution measurement with the CMS pixel detector"

15. A. Jaeger
    CMS Tracker Week, La Biodola, Isola d'Elba, Italy
    4 May 2010
    "Data comparison with Monte-Carlo"

16. A. Jaeger
    Annual meeting of the Swiss Physical Society, Basel, Switzerland
    22 June 2010
    "Performance of the CMS silicon pixel detector: results from the first data"

17. M. Ivova Rikova
    Annual meeting of the Swiss Physical Society, Basel, Switzerland
    21 June 2010
    "Measurement of the Lorentz angle in the CMS barrel pixel detector"

18. B. Millán Mejías
    Annual meeting of the Swiss Physical Society, Basel, Switzerland
    22 June 2010
    "Study of the $B_s$-meson with forthcoming data at the CMS detector

19. P. Otyugova
    CHIPP Workshop on the High Energy Frontier, Zurich
    1 September 2010
    "First CMS physics results"

20. C. Regenfus
    6th Patras Workshop on Axions, WIMPs and WISPs, Zurich

7 July 2010
"ArDM a ton scale LAr WIMP detector prototype"

21. C. Regenfus
Workshop on Antimatter Physics, Bergen, Norway
23 February 2011
"Relevant input and experience with Si-detectors from ATHENA"

22. T. Rommerskirchen
Annual meeting of the Swiss Physical Society, Basel, Switzerland
21 June 2010
"Supersymmetry at CMS with multijet events: an experimental strategy"

23. A. Schmidt
Kruger 2010: Workshop on Discovery Physics at the LHC, Kruger National Park (South Africa)
5 December 2010
"Performance of Track and Vertex Reconstruction and $B$-Tagging Studies with CMS in $pp$ Collisions at $\sqrt{s}$ =7 TeV"

24. A. Schmidt
Seminar given at the University of Freiburg i.B., Germany
15 February 2011
"$b$-quarks in the CMS experiment: from detector design to physics results"

25. H. Snoek
19th Int. Workshop on Vertex Detectors, Loch Lomond, Scotland
6 June 2010
"Beam backgrounds in the CMS pixel detector"

26. H. Snoek
6th Trento Workshop on Advanced Silicon Radiation Detectors, FBK–IRST, Trento
3 March 2011
"The CMS pixel detector: commissioning and performance"

27. J. Storey
Lecture given at the University of Bern
12 January 2011
"The AEgIS Inner Detector"

28. J. Storey
Workshop on Antimatter Physics, Bergen, Norway
22 February
"Central detector: possible technologies"

**AEgIS Collaboration (2010)**:
LAPP (Annecy), Queens U (Belfast), INFN Bescia - Firenze - Genova - Milano - Padova - Pavia - Trento, CERN, MPI-K (Heidelberg), Kirchoff Inst. of Phys (Heidelberg), INR (Moscow), ITEP (Moscow), Univ. Claude Bernard (Lyon), New York Univ., Univ. of Oslo, Univ. of Bergen, Czech Tech. Univ (Prague), IRNE (Sofia), ETH-Zurich, Qatar Univ., Politecnico Milano, Laboratoire Aimé Cotton (Orsay), Univ. of Zurich.

**ArDM Collaboration (2010)**:
C. Amsler, A. Badertscher, V. Boccone, A. Bueno, M.C. Carmona-Benitez, W. Creus, A. Curioni, M. Daniel, E. J. Dawe, U. Degunda, A. Gendotti, L. Epprecht, S. Horikawa, L. Kaufmann, L. Knecht, M. Laffranchi, C. Lazzaro, P. K. Lightfoot, D. Lussi, J. Lozano, A. Marchionni, K. Mavrokoridis, A. Melgarejo, P. Mijakowski, G. Natterer, S. Navas-Concha, P. Otyugova, M. de Prado, P. Przewlocki, C. Regenfus, F. Resnati, M. Robinson, J. Rochet, L. Romero, E. Rondio, A. Rubbia, L. Scotto-Lavina, N.J.C. Spooner, T. Strauss, J. Ulbricht, and T. Viant.

**CMS Collaboration**:
see http://cms.web.cern.ch/cms/Collaboration/Institutes/index.html

**DARWIN Collaboration**:
Subatech (France), University of Münster, MPIK Heidelberg, University of Karlsruhe, University of Mainz, INFN (LNGS - Torino - Napoli - Padova - Pavia -Milano), NIKHEF, University of Zurich, ETH-Zurich, Columbia University, Princeton University, UCLA.

**DIRAC Collaboration (2010)**:
B. Adeva, L. Afanasyev, Y. Allkofer, C. Amsler, A. Anania, A. Benelli, V. Brekhovskikh, G. Caragheorgheopol, T. Cechak, M. Chiba, P. Chliapnikov, C. Ciocarlan, S. Constantinescu, C. Curceanu, C. Detraz, D. Dreossi, D. Drijard, A. Dudarev, M. Duma, D. Dumitriu, J.L. Fungueiriño, J. Gerndt, A. Gorin, O. Gorchakov, K. Gritsay, C. Guaraldo, M. Gugiu, M. Hansroul, Z. Hons, S. Horikawa, M. Iliescu, V. Karpukhin, J. Kluson, M. Kobayashi, V. Komarov, V. Kruglov, L. Kruglova, A. Kulikov, A. Kuptsov, I. Kurochkin, K.-I. Kuroda, A. Lamberto, A. Lanaro, V. Lapshin, R. Lednicky, P. Levi Sandri, A. Lopez Aguera, V. Lucherini, I. Manuilov, C. Mariñas, L. Nemenov, M. Nikitin, K. Okada, V. Olchevskii, M. Pentia, A. Penzo, M. Pló, G.F. Rappazzo, C. Regenfus, J. Rochet, A. Romero, V. Ronjin, A. Ryazantsev, V. Rykalin, J. Saborido, J. Schacher, A. Sidorov, J. Smolik, S. Sugimoto, F. Takeutchi, A. Tarasov, L. Tauscher, T. Trojek, S. Trusov, V. Utkin, O. Vázquez Doce, T. Vrba, V. Yazkov, Y. Yoshimura, M. Zhabitsky, P. Zrelov.

**PARTICLE DATA Group (2010)**:
K. Nakamura, K. Hagiwara, K. Hikasa, H. Murayama, M. Tanabashi, T. Watari, C. Amsler, M. Antonelli, D. M. Asner, H. Baer, H. R. Band, R. M. Barnett, T. Basaglia, E. Bergren, J. Beringer, G. Bernardi, W. Bertl, H. Bichsel, O. Biebel, E. Blucher, S. Blusk, R. N. Cahn, M. Carena, A. Ceccucci, D. Chakraborty, M. -C. Chen, R. S. Chivukula, G. Cowan, O. Dahl, G. D'Ambrosio, T. Damour, D. de Florian, A. de Gouvea, T. DeGrand, G. Dissertori, B. Dobrescu, M. Doser, M. Drees, D. A. Edwards, S. Eidelman, J. Erler, V. V. Ezhela, W. Fetscher, B. D. Fields, B. Foster, T. K. Gaisser, L. Garren, H. -J. Gerber, G. Gerbier, T. Gherghetta, G. F. Giudice, S. Golwala, M. Goodman, C. Grab, A. V. Gritsan, J. -F. Grivaz, D. E. Groom, M. Grnewald, A. Gurtu, , T. Gutsche, H. E. Haber, C. Hagmann, K. G. Hayes, M. Heffner, B. Heltsley, J. J. Hernndez-Rey, A. Höcker, J. Holder, J. Huston, J. D. Jackson, K. F. Johnson, T. Junk, A. Karle, D. Karlen, B. Kayser, D. Kirkby, S. R. Klein, C. Kolda, R. V. Kowalewski, B. Krusche, Yu. V. Kuyanov, Y. Kwon, O. Lahav, P. Langacker, A. Liddle, Z. Ligeti, C. -J. Lin, T. M. Liss, L. Littenberg, K. S. Lugovsky, S. B. Lugovsky, J. Lys, H. Mahlke, T. Mannel, A. V. Manohar, W. J. Marciano, A. D. Martin, A. Masoni, D. Milstead, R. Miquel, K. Mnig, M. Narain, P. Nason, S. Navas, P. Nevski, Y. Nir, K. A. Olive, L. Pape, C. Patrignani, J. A. Peacock, S. T. Petcov, A. Piepke, G. Punzi, A. Quadt, , S. Raby, G. Raffelt, B. N. Ratcliff, P. Richardson, S. Roesler, S. Rolli, A. Romaniouk, L. J. Rosenberg, J. L. Rosner, C. T. Sachrajda, Y. Sakai, G. P. Salam, S. Sarkar, F. Sauli, O. Schneider, K. Scholberg, D. Scott, W. G. Seligman, M. H. Shaevitz, M. Silari, T. Sjstrand, J. G. Smith, G. F. Smoot, S. Spanier, H. Spieler, A. Stahl, T. Stanev, S. L. Stone, T. Sumiyoshi, M. J. Syphers, J. Terning, M. Titov, N. P. Tkachenko, N. A. Trnqvist,

D. Tovey, T. G. Trippe, G. Valencia, K. van Bibber, G. Venanzoni, M. G. Vincter, P. Vogel, A. Vogt, W. Walkowiak, C. W. Walter, D. R. Ward, B. R. Webber, G. Weiglein, E. J. Weinberg, J. D. Wells, A. Wheeler, L. R. Wiencke, C. G. Wohl, L. Wolfenstein, J. Womersley, C. L. Woody, R. L. Workman, A. Yamamoto, W. -M. Yao, O. V. Zenin, J. Zhang, R. -Y. Zhu P. A. Zyla .